creative commons

COMMONS DEED

저작자표시-비영리-변경금지 2.0 대한민국

이용자는 아래의 조건을 따르는 경우에 한하여 자유롭게

- 이 저작물을 복제, 배포, 전송, 전시, 공연 및 방송할 수 있습니다.

다음과 같은 조건을 따라야 합니다:

저작자표시. 귀하는 원저작자를 표시하여야 합니다.

비영리. 귀하는 이 저작물을 영리 목적으로 이용할 수 없습니다.

변경금지. 귀하는 이 저작물을 개작, 변형 또는 가공할 수 없습니다.

- 귀하는, 이 저작물의 재이용이나 배포의 경우, 이 저작물에 적용된 이용허락조건을 명확하게 나타내어야 합니다.
- 저작권자로부터 별도의 허가를 받으면 이러한 조건들은 적용되지 않습니다.

저작권법에 따른 이용자의 권리는 위의 내용에 의하여 영향을 받지 않습니다.

이것은 이용허락규약(Legal Code)을 이해하기 쉽게 요약한 것입니다.

Disclaimer

dCollection

이학박사 학위논문

Anatomically-guided PET reconstruction: from non-smooth prior to a deep learning approach

해부학적 유도 **PET** 재구성:
매끄럽지 않은 사전 함수부터
딥러닝 접근까지

2020 년 10 월

서울대학교 대학원
의과학과

강 승 관

Thesis for the Degree of
Doctor of Philosophy in Science

Anatomically-guided PET reconstruction: from non-smooth prior to a deep learning approach

해부학적 유도 PET 재구성:
매끄럽지 않은 사전 함수부터
딥러닝 접근까지

September 2020

Seoul National University Graduate School
Major in Biomedical Sciences

Seung Kwan Kang

해부학적 유도 PET 재구성: 매끄럽지 않은 사전 함수부터 딥러닝 접근까지

지도 교수 이 재 성

이 논문을 이학박사 학위논문으로 제출함

2020 년 10 월

서울대학교 대학원

의과학과

강 승 관

강승관의 이학박사 학위논문을 인준함

2021 년 1 월

위 원 장 _____ 강 명 주 _____ (인)

부위원장 _____ 이 재 성 _____ (인)

위 원 _____ 이 인 아 _____ (인)

위 원 _____ 김 현 진 _____ (인)

위 원 _____ 전 세 영 _____ (인)

Abstract

Anatomically-guided PET reconstruction: from non-smooth prior to a deep learning approach

Seung Kwan Kang
Major in Biomedical Sciences
Department of Biomedical Sciences
Seoul National University Graduate School

Advances in simultaneous positron emission tomography/magnetic resonance imaging (PET/MRI) technology have led to an active investigation of the anatomy-guided regularized PET image reconstruction algorithm based on MR images. Among the various priors proposed for anatomy-guided regularized PET image reconstruction, Bowsher's method based on second-order smoothing priors sometimes suffers from over-smoothing of detailed structures. Therefore, in this study, we propose a Bowsher prior based on the l_1 norm and an iteratively reweighting scheme to overcome the limitation of the original Bowsher method. In addition, we have derived a closed solution for iterative image reconstruction based on this non-smooth prior. A comparison study between the original l_2 and proposed l_1 Bowsher priors were conducted using computer simulation and real human data. In the simulation and real data application, small lesions with abnormal PET uptake were better detected by the proposed l_1 Bowsher prior methods than the original

Bowsher prior. The original l_2 Bowsher leads to a decreased PET intensity in small lesions when there is no clear separation between the lesions and surrounding tissue in the anatomical prior. However, the proposed l_1 Bowsher prior methods showed better contrast between the tumors and surrounding tissues owing to the intrinsic edge-preserving property of the prior which is attributed to the sparseness induced by l_1 norm, especially in the iterative reweighting scheme. Besides, the proposed methods demonstrated lower bias and less hyper-parameter dependency on PET intensity estimation in the regions with matched anatomical boundaries in PET and MRI.

Moreover, based on the formulation of l_1 Bowsher prior, the unrolled network containing the conventional maximum-likelihood expectation-maximization (ML-EM) module was also proposed. The convolutional layers successfully learned the distribution of anatomically-guided PET images and the EM module corrected the intermediate outputs by comparing them with sinograms. The proposed unrolled network showed better performance than ordinary U-Net, where the regional uptake is less biased and deviated. Therefore, these methods will help improve the PET image quality based on the anatomical side information.

Keywords: image reconstruction, positron emission tomography, anatomical prior, regularization, deep learning, unrolled network

Student Number: 2014-22024

Table of Contents

Chapter 1. Introduction 1

1.1. Backgrounds 1

1.1.1. Positron Emission Tomography 1

1.1.2. Maximum a Posterior Reconstruction 1

1.1.3. Anatomical Prior 2

1.1.4. Proposed l_1 Bowsher Prior 3

1.1.5. Deep Learning for MR-less Application 4

1.2. Purpose of the Research 4

Chapter 2. Anatomically-guided PET Reconstruction Using Bowsher Prior 6

2.1. Backgrounds 6

2.1.1. PET Data Model 6

2.1.2. Original Bowsher Prior 7

2.2. Methods and Materials 8

2.2.1. Proposed l_1 Bowsher Prior 8

2.2.2. Iterative Reweighting 13

2.2.3. Computer Simulations 15

2.2.4. Human Data 16

2.2.5. Image Analysis 17

2.3. Results 19

2.3.1. Simulation with Brain Phantom 19

2.3.2.Human Data 20

2.4. Discussions 25

Chapter 3. Deep Learning Approach for Anatomically-guided PET Reconstruction 31

3.1. Backgrounds 31

3.2. Methods and Materials 33

3.2.1. Douglas-Rachford Splitting 33
3.2.2. Network Architecture 34
3.2.3. Dataset and Training Details 35
3.2.4. Image Analysis 36
3.3. Results 37
3.4. Discussions 38

Chapter 6. Conclusions 40

Bibliography 41

Abstract in Korean (국문 초록) 52

Table of Figures

Figure 1-1. Simple schematic of iterative reconstruction 2
Figure 2-1. Example of the proposed proximal operator 10
Figure 2-2. Simulated brain phantoms 15
Figure 2-3. The representative reconstructed images for low noise-level 18
Figure 2-4. The representative reconstructed images for high noise-level 18
Figure 2-5. Bias map for low noise-level 20
Figure 2-6. Bias map for high noise-level 21
Figure 2-7. Bias-STD plot of computer simulation results 22
Figure 2-8. Reconstructed brain [^{18}F]FDG images 23
Figure 2-9. Regional analysis for brain [^{18}F]FDG images 24
Figure 2-10. Reconstructed head and neck tumor patient images 25
Figure 2-11. Quantitative analysis for head and neck tumor patient images 25
Figure 2-12. Comaprison with TV reconstruction without anatomical parior 29
Figure 3-1. Schematic of the unrolled deep neural network 35
Figure 3-2. Reconstructed brain PET images 36
Figure 3-3. RMSE and SSIM evluations 37
Figure 3-4. Bland-Altman plot of regional gray matter activity 38

Chapter 1. Introduction

1.1 Backgrounds

1.1.1 Positron Emission Tomography

Positron emission tomography (PET) is a medical imaging device that is highly sensitive in identifying functional and molecular abnormalities in patients with various diseases. For PET imaging, radiopharmaceuticals emitting positrons are synthesized and injected into the patient's body. PET has the advantage of being able to non-invasively investigate detailed functional activities of the human body. The emitted positrons travel to nearby tissues in a short length (< 1 mm), and interact with the electrons. The interaction of positron and electron results in a pair of annihilation gamma photons moving in approximately opposite directions. To measure the annihilation photons, scintillation detectors consisting of scintillation crystals and photosensors, such as photomultiplier tube (PMT) and silicon photomultiplier (SiPM), are employed in PET systems [1]. Coincidence events are recorded by a PET scanner using a coincidence detection module. Finally, the tomographic images are obtained by applying image reconstruction algorithms to the coincidence data. Clinically, various filters are applied to the reconstructed images to obtain better quality.

1.1.2. Maximum A Posteriori Reconstruction

However, PET images have lower spatial resolution and higher noise levels compared to anatomical imaging modalities, such as computed tomography (CT) and magnetic resonance imaging (MRI). Numerous mathematical and computational

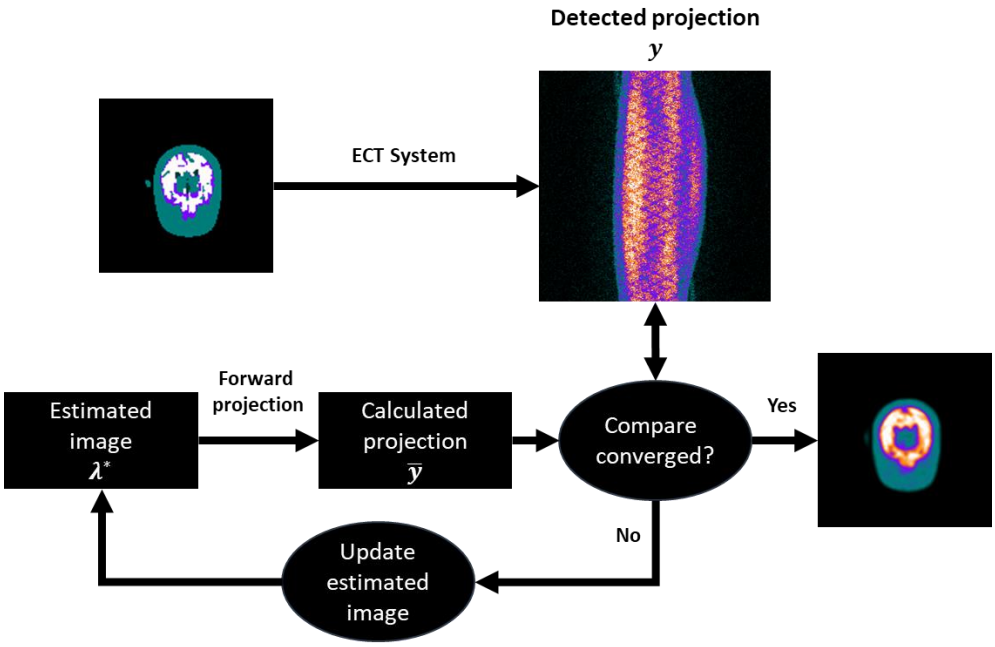

Figure 1-1. A simple schematic of iterative reconstruction. The figure describes the maximum-likelihood expectation-maximization algorithm (ML-EM).

methods, including iterative reconstruction algorithms accounting for the noise properties of measured data have been developed to improve the image quality and quantitative accuracy of the PET [2-4] (Figure 1-1). The formulation of optimization problems based on Poisson statistics for iterative PET image reconstruction is generally ill-posed in high-noise circumstances, resulting in inconsistent solutions with no certainty of convergence [5-7]. To mitigate such problems, maximum a posteriori (MAP) reconstruction algorithms, also known as penalized likelihood reconstruction methods, are used. MAP reconstruction allows the solution to stabilize by incorporating prior information into the optimization problem formulation [8-12]. Nonetheless, smoothing priors (e.g., the quadratic prior) used for reducing noise in reconstructed images also eliminate some essential high-frequency features, such as anatomical edges and small lesions.

1.1.3. Anatomical Prior

To preserve the anatomical edges and small lesions during the reconstruction process, we can use edge-preserving priors, such as the non-local means prior [13]. Alternatively, anatomical information provided by CT or MRI can be utilized as a prior (anatomically-guided PET image reconstruction) [14-22]. In recent years, advances in simultaneous PET/MRI technology [23-27] have led to an active investigation of such anatomically-guided PET image reconstruction algorithms based on MR images. MRI with higher soft-tissue contrast compared to CT would be a useful anatomic prior, particularly for brain and head/neck regions. Either raw MR images or segmentation outcomes can be used as the priors for PET image reconstruction [28-32]. This study focuses on the former method because the segmentation-based method is vulnerable to segmentation error.

1.1.4. Proposed l_1 Bowsher Prior

Among the various priors proposed for anatomy-guided regularized PET image reconstruction, Bowsher's method is one of the best performing anatomical priors [22, 33]. However, the original Bowsher's method based on second-order smoothing prior sometimes suffers from over-smoothing of detailed structures. Therefore, in this study, we propose a Bowsher prior based on the l_1 norm to overcome the limitation of the original Bowsher method. An interesting property of newly derived prior is that it induces sparseness of the image like total-variation (TV) prior [34, 35]. Accordingly, we could improve the performance of the proposed prior by applying an iterative reweighting scheme introduced in [36]. A modified proximal gradient algorithm was used to solve the optimization problem of Poisson log-likelihood and

non-smooth prior. Computer simulation studies under different noise conditions were conducted to compare the performance of the original and proposed l_1 Bowsher priors. We also analyzed both priors using clinical [^{18}F]FDG PET images.

1.1.5. Deep Learning for MR-less Application

Nonetheless, the simultaneous PET/MRI scanner is not available in most clinical and research centers. Besides, not all the patients who undergo PET/CT scans have corresponding MR images. Therefore, we aimed to develop an MR-less application for anatomically guided PET reconstruction. We used deep learning to solve this problem, which developed a lot recently [37-41]. Once we have a dataset paired with PET and MR images, the anatomically guide PET reconstruction can be conducted. Reconstructed results are used as the reference target of the network training. We first examined the end-to-end training using U-Net [42]. However, this method does not consider the projection or back-projection modeling of the data. Accordingly, the test result can be distorted if input distribution is significantly different from the training set. In this research, we proposed to use an unrolled model containing the maximum-likelihood expectation-maximization (ML-EM) module in the neural network. Moreover, the proposed unrolled network is closely related to the optimization of the l_1 Bowsher prior, where the proximal operator is a substitute for the convolutional neural network.

1.2 Purpose of the Research

The first aim of the thesis is to develop anatomically-guided PET reconstruction using l_1 Bowsher prior, which is non-smooth. Secondly, the MR-less application of

anatomically-guided PET reconstruction is studied using an unrolled network combined with conventional ML-EM update and convolutional neural network.

In Chapter 2, we describe the general formulation of the reconstruction problem using penalized log-likelihood. The equations of the original Bowsher prior and its optimization method are also given. Moreover, a detailed description of proposed l_1 Bowsher prior and its iterative reweighting scheme is also provided.

In Chapter 3, the MR-less application of anatomically-guided PET reconstruction is presented. The proposed unrolled network is compared to ordinary U-Net. Detailed architecture and the dataset are also described.

In Chapter 4, we summary our researches.

Chapter 2. Anatomically-guided PET reconstruction using Bowsher Prior

2.1. Backgrounds

2.1.1. PET Data Model

The Poisson log-likelihood model is used for PET image reconstruction to account for the statistical properties of PET image acquisition [3, 4]. However, the maximum log-likelihood solution for unknown images usually yields noisy results because the problem is fundamentally ill-posed. Thus, regularization is considered to recover better images by imposing some appropriate assumptions. The penalized negative log-likelihood estimate of the unknown image $\boldsymbol{x}$ is expressed as:

$$\arg\min_{\boldsymbol{x}\geq 0} \sum_{i} \hat{y}_i(\boldsymbol{x}) - \boldsymbol{y}_i \log \hat{y}_i(\boldsymbol{x}) + \beta R(\boldsymbol{x}), \tag{1}$$

where y_i is the observed data for the ith line of response, $R(\cdot)$ is the penalty function, β is a weighting parameter of the penalty function, and $\hat{y}_i(\cdot)$ is a forward projection of the image to the i-th line of response. The expected count distribution $\hat{y}_i(\boldsymbol{x})$ for image $\boldsymbol{x}$ is expressed as $\hat{y}_i(\boldsymbol{x}) = A\boldsymbol{x} + \boldsymbol{s}$, where A is a system matrix and s denotes the expected distribution of random and scatter events. We can provide anatomical information available in the MR image to the penalty function $R(\cdot)$. As mentioned earlier, one of the popular choices for the penalty function $R(\cdot)$ is the Bowsher prior [33], which will be discussed in the following sections.

2.1.2. Original Bowsher Prior

The original Bowsher prior is expressed as [22, 33]

$$R_{l_2}(\boldsymbol{x}|\boldsymbol{z}) = \sum_j \sum_{l \in N_j} w_{lj} \left(\boldsymbol{x}_l - \boldsymbol{x}_j\right)^2 , \tag{2}$$

$$w_{lj} = \begin{cases} 1 & \forall \boldsymbol{z}_k \in B_j, \text{if } \left|\boldsymbol{z}_j - \boldsymbol{z}_l\right| < \left|\boldsymbol{z}_j - \boldsymbol{z}_k\right| \\ 0 & \text{else} \end{cases}, \tag{3}$$

where $\boldsymbol{z}$ is a prior MR image and N_j is the neighbor voxel of the *j*-th voxel. The weight $w_{\cdot j}$ uses the difference between the center of the MR image patch and its surrounding voxels to determine the smoothness in the homogenous region. If the difference is large, the boundary of the given image is preserved. B_j consists of the *k* most similar voxels in the anatomical image around the *j*-th voxel. In the previous study, authors showed that the modifying quadratic term in (2) to relative difference yielded better performance [15, 22, 43].

$$R_{l_2}^{rel} = \sum_j \sum_{l \in N_j} w_{lj} \frac{\left(\boldsymbol{x}_l - \boldsymbol{x}_j\right)^2}{\boldsymbol{x}_l + \boldsymbol{x}_j} \tag{4}$$

To reconstruct the image using this prior, we utilized the asymmetric Bowsher prior and one-step-late algorithm developed in [43, 44]. The meaning of "asymmetric" is that:

$$\frac{\partial R_{l_2}^{rel}}{\partial \boldsymbol{x}_j} = \sum_j \sum_{l \in N_j} w_{lj} \frac{\partial}{\partial \boldsymbol{x}_j} \left(\frac{\left(\boldsymbol{x}_l - \boldsymbol{x}_j\right)^2}{\boldsymbol{x}_l + \boldsymbol{x}_j} \right). \tag{5}$$

Note that additional term $\sum_j \sum_{l \in N_j} w_{jl} \frac{\partial}{\partial x_j} \left(\frac{(x_j - x_l)^2}{x_j + x_l} \right)$ is removed from the derivative. The second derivative is also modified as the above notation. Authors in [43, 44] showed that this modification yielded better performances. The update of each voxel $\boldsymbol{x}_j$ is expressed as the following equation:

$$\boldsymbol{x}_j^{n+1} = \boldsymbol{x}_j^n + \left(\frac{\partial L}{\partial \boldsymbol{x}_j} + \frac{\partial R_{l_2}^{rel}}{\partial \boldsymbol{x}_j}\right) / \left(\frac{a_j}{\boldsymbol{x}_j^n} - \frac{\partial^2 R_{l_2}^{rel}}{\partial \boldsymbol{x}_j^2}\right), \tag{6}$$

where L is the negative log-likelihood, and $a_j = \sum_j a_{ij}$ is the sum of the system matrix. This original Bowsher prior is a l_2-norm prior; therefore, it sometimes suffers from over-smoothing of detailed structures.

2.2. Methods and Materials

2.2.1. Proposed l_1 Bowhser Prior

Our proposed l_1 Bowsher prior is defined as follows:

$$R_{l_1}(\boldsymbol{x}|\boldsymbol{z}) = \sum_j \sum_{l \in N_j} w_{lj} |\boldsymbol{x}_l - \boldsymbol{x}_j| \,. \tag{7}$$

Instead of using a squared function between the center voxel and its neighbors, the l_1 norm was exploited. This prior is convex but not smooth. Therefore, we devised a modified proximal gradient algorithm because the reconstruction scheme from the original Bowsher prior was not applicable. At first, the EM update equation can also

be described as [45]

$$\boldsymbol{x}^{n+1} = \boldsymbol{x}^{n} - D(\boldsymbol{x}^{n})\nabla L(\boldsymbol{x}^{n}), \tag{8}$$

where $D(\boldsymbol{x}^{n}) = diag(\boldsymbol{x}^{n}/A^{T}\mathbf{1})$, and $A^{T}\mathbf{1}$ is the backprojection of a vector whose elements are equal to 1. Thus, $\boldsymbol{x}^{n+1}$ is the solution to the following problem:

$$\begin{aligned} &\text{aargmin}_{\boldsymbol{x}}\, L(\boldsymbol{x}^{n}) + \nabla L(\boldsymbol{x}^{n})^{T}(\boldsymbol{x} - \boldsymbol{x}^{n}) + \frac{1}{2}\|\boldsymbol{x} - \boldsymbol{x}^{n}\|^{2}_{D(\boldsymbol{x}^{n})^{-1}} \\ &= \text{argmin}_{\boldsymbol{x}}\, \frac{1}{2}\|\nabla L(\boldsymbol{x}^{n})\|^{2}_{D(\boldsymbol{x}^{n})^{-1}} + \nabla L(\boldsymbol{x}^{n})^{T}(\boldsymbol{x} - \boldsymbol{x}^{n}) \\ &\qquad + \frac{1}{2}D\|\boldsymbol{x} - \boldsymbol{x}^{n}\|^{2}_{D(\boldsymbol{x}^{n})^{-1}} \\ &= \text{argmin}_{\boldsymbol{x}}\, \tfrac{1}{2}\|\boldsymbol{x} - \boldsymbol{x}^{n} + D(\boldsymbol{x}^{n})\nabla L(\boldsymbol{x}^{n})\,\|^{2}_{D(\boldsymbol{x}^{n})^{-1}}.. \end{aligned} \tag{9}$$

In the (9), the $L(\boldsymbol{x}^{n})$ can be removed because it does not depend on $\boldsymbol{x}$ and $1/2\|\nabla L(\boldsymbol{x}^{n})\|^{2}_{D(\boldsymbol{x}^{n})^{-1}}$ can be inserted into the first equation for the same reason. This equation can be regarded as the second-order Taylor approximation of Poisson log-likelihood where the Hessian is substituted for $D(\boldsymbol{x}^{n})^{-1}$. Consequently, we can rewrite the original problem (1) in the following approximated form after combining the proposed regularization term:

$$\text{argmin}_{\boldsymbol{x}\geq 0}\, \tfrac{1}{2}\|\boldsymbol{x} - \boldsymbol{x}^{n+1}\|^{2}_{D(\boldsymbol{x}^{n})^{-1}} + \beta R_{l_1}(\boldsymbol{x}|\boldsymbol{z}). \tag{10}$$

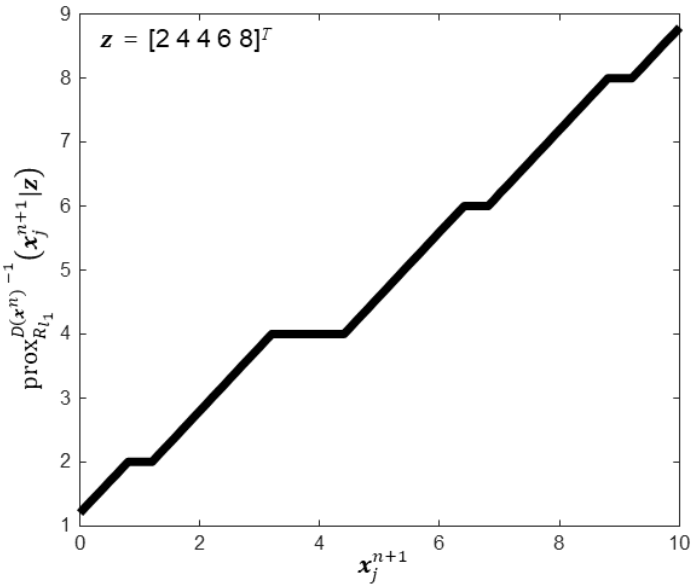

Figure 2-1. Example of the proposed proximal operator

This formula is the modified proximal mapping for a penalty function R_{l_1}, where $D(\boldsymbol{x}^n)^{-1}$ plays the role of diagonal weighting. The proximal gradient algorithm is efficient when a closed expression of the proximal mapping is provided. We were able to determine the proximal mapping for the individual voxel $\boldsymbol{x}_j$ by applying the subgradient optimality condition [46] (see Figure 2-1).

$$0 \in \partial\left(\frac{1}{2d_j}\left(\boldsymbol{x}_j - \boldsymbol{x}_j^{n+1}\right)^2 + \beta\left(\sum_{l\in N_j} w_{lj}\left|\boldsymbol{x}_l - \boldsymbol{x}_j\right| + \sum_{m\in N_j} w_{jm}\left|\boldsymbol{x}_j - \boldsymbol{x}_m\right|\right)\right) \tag{11}$$

The final term $\sum_{m\in N_j} w_{jm}\left|\boldsymbol{x}_j - \boldsymbol{x}_m\right|$ is included for the symmetricity of the

proposed prior. If we remove this term, it becomes asymmetric l_1 Bowsher prior. We used the asymmetric l_1 Bowsher in this study. The solution of the subgradient is given by if we set $\boldsymbol{x}_i \neq \boldsymbol{x}_j$ for $i,j \in N_j$ and $\boldsymbol{x}_i < \boldsymbol{x}_j$ for $\forall\ i < j$:

$$\partial\left(\sum_{l\in N_j} w_{lj}|\boldsymbol{x}_l - \boldsymbol{x}_j|\right) = \begin{cases} -\sum_{l\in N_j} w_{lj} & \text{if } \boldsymbol{x}_j < \boldsymbol{x}_1 \\ \vdots & \\ w_i[-1,1] + \sum_{l=1}^{i-1} w_{lj} - \sum_{l=i+1}^{n_l} w_{lj} & \text{if } \boldsymbol{x}_j = \boldsymbol{x}_i \\ \sum_{l=1}^{i} w_{lj} - \sum_{l=i+1}^{n_l} w_{lj} & \text{if } \boldsymbol{x}_i < \boldsymbol{x}_j < \boldsymbol{x}_{i+1} \\ \vdots & \\ \sum_{l\in N_j} w_{lj} & \text{if } \boldsymbol{x}_j > \boldsymbol{x}_{n_l} \end{cases} \tag{12}$$

Rearranging (12) yields the following solution:

$$\operatorname{prox}_{R_{l_1}}^{D(\boldsymbol{x}^n)^{-1}}\left(\boldsymbol{x}_j^{n+1}|\boldsymbol{z}\right) = \begin{cases} \boldsymbol{x}_j^{n+1} + d_j\beta \sum_{l\in N_j} w_{lj} & \text{if } \boldsymbol{x}_j^{n+1} \in S_1^+ \\ \vdots & \\ \boldsymbol{x}_i & \text{if } \boldsymbol{x}_j^{n+1} \in S_i^- \\ \boldsymbol{x}_j^{n+1} - d_j\beta \sum_{l=1}^{i} w_{lj} & \\ +d_j\beta \sum_{l=i+1}^{n_l} w_{lj} & \text{if } \boldsymbol{x}_j^{n+1} \in S_i^+ \\ \vdots & \\ \boldsymbol{x}_j^{n+1} - d_j\beta \sum_{l\in N_j} w_{lj} & \text{if } \boldsymbol{x}_j^{n+1} \in S_{n_l}^+ \end{cases} \tag{13}$$

where n_l is the number of elements in the set N_j, $2 \le i \le n_l - 1$, and

$$
\begin{aligned}
S_1^+ &= \left\{ u \middle| u \le \boldsymbol{x}_1 - d_j \beta \textstyle\sum_{l \in N_j} w_{lj} \right\} \\
&\vdots \\
S_i^- &= \left\{ u \middle| \begin{array}{l} \boldsymbol{x}_i + d_j \beta \left(\sum_{l=1}^{i-1} w_{lj} - \sum_{l=i+1}^{n_l} w_{lj} - w_{li} \right) < u \\ \le \boldsymbol{x}_i + d_j \beta \left(\sum_{l=1}^{i-1} w_{lj} - \sum_{l=i+1}^{n_l} w_{lj} + w_{li} \right) \end{array} \right\} \\
S_i^+ &= \left\{ u \middle| \begin{array}{l} \boldsymbol{x}_i + d_j \beta (\sum_{l=1}^{i} w_{lj} - \sum_{l=i+1}^{n_l} w_{lj}) < \\ u \le \boldsymbol{x}_{i+1} + d_j \beta (\sum_{l=1}^{i} w_{lj} - \sum_{l=i+1}^{n_l} w_{lj}) \end{array} \right\} \\
&\vdots \\
S_{n_l}^+ &= \left\{ u \middle| u > \boldsymbol{x}_{n_l} + d_j \beta \textstyle\sum_{l \in N_j} w_{lj} \right\}.
\end{aligned}
\tag{14}
$$

Note that $S_1^+ \cup \cdots \cup S_i^- \cup S_i^+ \cup \cdots \cup S_{n_l}^+ = \mathbb{R}$ and each $S_\cdot^\cdot$ is disjoint sets. The example of proximal mapping is presented in Figure 2-1, and it is similar to the soft thresholding operator [47]. Therefore, image reconstruction with the proposed l_1 Bowsher prior is conducted by applying the EM update (8) followed by the modified proximal operator update (13). Both the original and proposed Bowsher prior reconstruction algorithms can be accelerated by replacing the EM update with the ordered subset (OS) algorithm.

Algorithm 1. Modified proximal gradient with ordered subsets

```
input y and z
initialize x
for n_1 = 1...n_out do
    for n_2 = 1 ... n_subsets do
        x^EM = x − D(x)∇L_{n_2}(x)  (ordinary EM using subsets)
            for j = 1 ... n_j do
                x^EM_{j,prox} = prox^{D(x_j)^{-1}}_{R_{l_1}}(x^EM_j | z)  (proximal operator)
            set x = x^EM_prox
        end
    end
return
```

2.2.2. Iterative Reweighting

Proposed l_1 Bowsher prior (7) is similar to TV-l_1 regularization which is one of the sparsity-inducing methods [34, 35]. Thus, we can apply the iterative reweighting method to further enforce the sparsity of the proposed l_1 Bowhser prior [36]. The modified prior is given by:

$$R_{l_1}^{IR}(\boldsymbol{x}|\boldsymbol{z}) = \sum_j \sum_{l \in N_j} w_{lj}^{IR} w_{lj} |\boldsymbol{x}_l - \boldsymbol{x}_j| \,, \tag{15}$$

$$w_{lj}^{IR} = \frac{1}{w_{lj}|\boldsymbol{x}_l - \boldsymbol{x}_j| + \epsilon}, \tag{16}$$

where $\epsilon > 0$ is the design parameter that controls the stability of the algorithm, which yields relatively consistent results for its variation [36]. In our experiments, $\epsilon = 0.1$ was used for both simulation and clinical dataset. For the optimization, the weights w_{lj} of proximal operator (13) at each iteration n is modified to

Algorithm 2. OS-Modified proximal gradient with iteratively reweighting

```
input y and z
initialize x
    for n_1 = 1 ... n_out do
        for n_2 = 1 ... n_subsets do
            x^EM = x − D(x)∇L_{n_2}(x)
                for j = 1 ... n_j do
                    if n_1 = 1
                        x^EM_{j,prox} = prox^{D(x_j)^{-1}}_{R_{l_1}}(x^EM_j | z)  (eq. (12))
                        set x = x^EM_prox
                    else
                        x^EM_{j,prox} = prox^{D(x_j)^{-1}}_{R^IR_{l_1}}(x^EM_j | z)  (eq. (12) with weight (16))
                        set x = x^EM_prox
                    end
                end
        End
    end
return
```

$$w_{lj}^{IR,n} = \frac{1}{w_{lj}|\boldsymbol{x}_l^n - \boldsymbol{x}_j^n| + \epsilon}, \tag{17}$$

which means that the weight of current iteration is calculated using the previous images. As in the [36], the iteratively reweighted prior is originated from the majorization-minimization (MM) algorithm of the following log-concave prior:

$$R_{log}^{IR}(\boldsymbol{x}|\boldsymbol{z}) = \sum_j \sum_{l \in N_j} \log(w_{lj}^{IR}|\boldsymbol{x}_l - \boldsymbol{x}_j| + \epsilon)\,. \tag{18}$$

Accordingly, the optimization problem is not convex anymore, so that the convergence to a global solution is not guaranteed. Therefore, the proper initial condition is important and we start this iteratively reweighting scheme after one

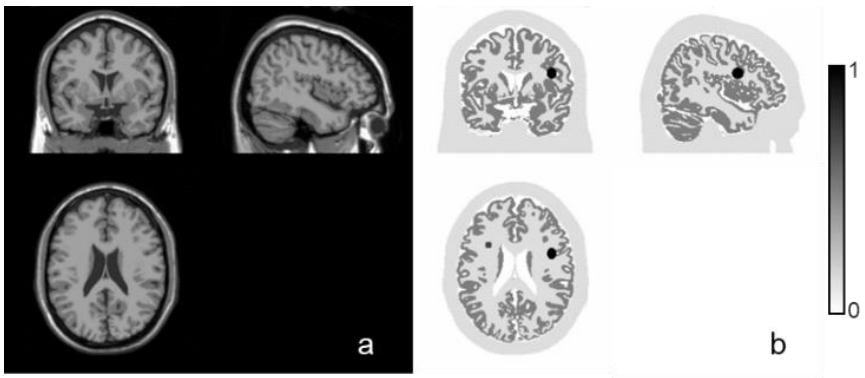

Figure 2-2. Simulated brain phantoms. a. MRI and b. PET.

iteration of the OS algorithm. This approach did not cause convergence problems, at least in our experiments.

2.2.3. Computer Simulations

We generated the ground truth PET image based on the MR image and its segmentations obtained from BrainWeb [48, 49]. The image was divided into four regions: gray matter (GM), white matter and others (WM, and so on), small tumor, and large tumor. We assigned image intensities of 0.5, 0.125, 0.75, and 1 to each of these regions (Figure 2-2). The attenuation map was also generated from the ground truth image and a scatter map was acquired by filtering the projections with 50 mm Gaussian FHWM. Two different levels of Poisson noise was added to the projections assuming two different situations: 5 min acquisition (total 7.0×10^7 prompt counts) and 1 min acquisition (total 1.4×10^7 prompt counts) using Siemens Biograph mMR system (Siemens Healthcare, Knoxville, TN), where the number of views in the sinogram was 168. To analyze the results statistically, 15 independent noise realizations are produced. We compared three different image reconstruction strategies: original l_2 Bowsher prior with a relative difference, proposed l_1 Bowsher prior and l_1 Bowsher prior with iterative reweighting. The initial

conditions for all the compared algorithms were the output of the first iteration of OS-EM. The OS algorithm had 21 subsets and the number of outer iterations was 6. The Bowsher prior was calculated in the nearest 80 voxels. Although the previous report showed the optimal number of selected voxels in the patch (k) was about 10 [15, 43], we also examined the larger patch size (20). The regularization parameters for the original Bowsher prior were from 0.1×2^0 to 0.1×2^7 with logarithmic scale 2, and those for the proposed l_1 Bowsher prior were 0.1×2^1 to 0.1×2^8 divided into the same logarithmic scale.

2.2.4. Human Data

The proposed method was applied to two different sets of human data acquired using the Siemens Biograph mMR system. One of them was obtained from the PET/MRI scan of a healthy volunteer (59 years old male) acquired 110 min after the injection of 192 MBq [^{18}F]FDG. The PET scan duration was 10 min. A T1-weighted structural MRI was also acquired using the ultrafast gradient-echo sequence and reconstructed into a $208 \times 256 \times 256$ matrix with voxel sizes of $1.0 \times 0.98 \times 0.98$ mm [50].

The other set was the PET/MRI data of a patient with head and neck cancer 76 years old female). Both T1- and T2-weighted MRIs were acquired using a turbo spin-echo sequence, whereas the [^{18}F]FDG PET scan was obtained after 110 min after injection of 256 MBq of the radiotracer. Of the MRIs, only T1-weighted MR images were used for the regularized PET reconstruction. Retrospective use of all human data was approved by the Institutional Review Board of our institute.

Deep learning-based super-resolution along the z-axis was performed because the slice thickness of the acquired MR image was thicker than that of the PET scan [51]. The SPM12 (SPM12; University of College London, UK) program was used

to re-slice the MR images to have the same voxel size and dimension as that of the PET scan. The Fourier rebinning algorithm was applied to the PET sinogram data, and 2D projection and the backprojection algorithm were used [52]. The same regularization parameters or post-filters as those used in the computer simulation were applied. The number of voxels selected within the patch was fixed at 20, which was showed quantitatively better performances in the simulation study.

2.2.5. Image Analysis

Standard deviation (STD) and bias in the PET image intensity were calculated for each region in the simulation study:

$$\mathrm{STD} = \sqrt{\frac{\sum_i \left(\boldsymbol{x}_{\mathrm{GT,i}}^{\mathrm{region}} - \boldsymbol{x}_{\mathrm{recon,i}}^{\mathrm{region}}\right)^2}{n^{\mathrm{region}} - 1}}, \tag{19}$$

$$\mathrm{Bias}^{\mathrm{region}} = \frac{1}{n}\sum_i \boldsymbol{x}_{\mathrm{GT,i}}^{\mathrm{region}} - \boldsymbol{x}_{\mathrm{recon,i}}^{\mathrm{region}}, \tag{20}$$

where $\boldsymbol{x}_{\mathrm{recon}}$ is a reconstructed image of the given region (GM, WM, and tumors), $\bar{\boldsymbol{x}}_{\mathrm{recon}}^{\mathrm{region}}$ is the mean value over the given region, n^{region} is the number of voxels, and $\boldsymbol{x}_{\mathrm{GT}}^{\mathrm{region}}$ is the ground truth value of each region.

From the [^{18}F]FDG brain PET of a healthy volunteer, we calculated the mean uptake level (kBq/ml) in the frontal lobe, cingulate cortex, superior parietal gyrus, and lateral temporal gyrus using regions of interest (ROI) drawn only on the gray matter pixels shown in the MRI. The SPM12 program was used to extract gray matter and above ROIs were defined in AAL template [53, 54]. The standard deviation of the uptake level in the white matter that has the most homogenous uptake in the brain

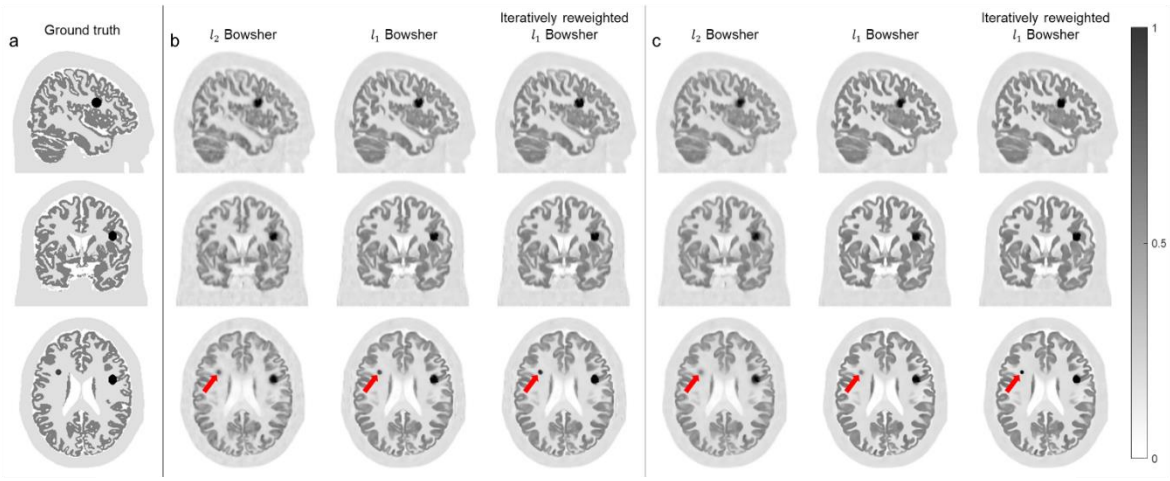

Figure 2-3. The representative reconstructed images using original l_2 Bowsher prior, proposed l_1 Bowsher prior and its iterative reweighting variation under low-level noise circumstances (total 7.0×10^7 prompt counts). Red arrow indicates the position of small lesions. a. Ground truth, b. 10 voxels selection in the given patch (nearest 80 voxels) and c. 20 voxels selections in the given patch.

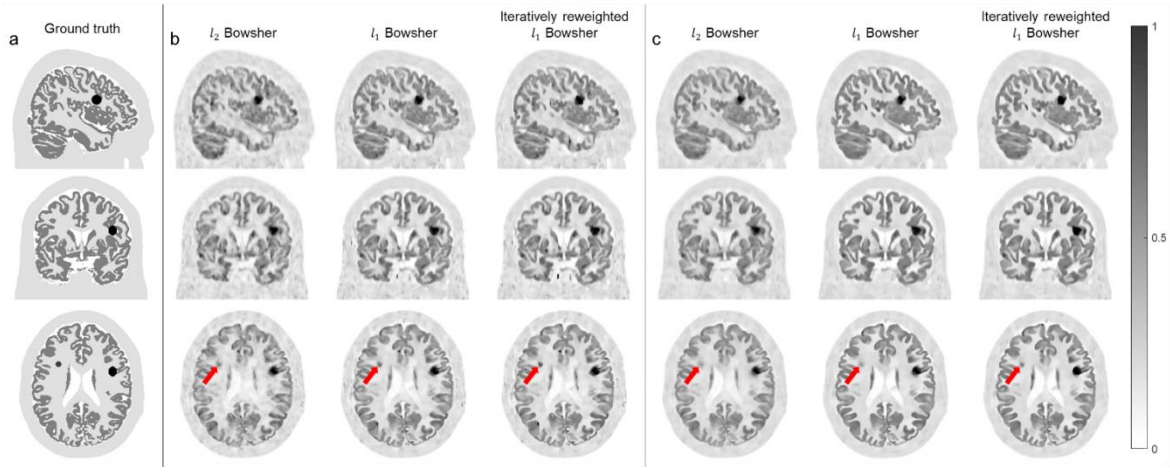

Figure 2-4. The representative reconstructed images using original l_2 Bowsher prior, proposed l_1 Bowsher prior and its iterative reweighting variation under high-level noise circumstances (total 1.4×10^7 prompt counts). Red arrow indicates the position of small lesions. a. Ground truth, b. 10 voxels selection in the given patch (nearest 80 voxels) and c. 20 voxels selections in the given patch.

was also calculated. We focused on two lesions (large and small) with high uptake in the patient with head and neck cancer.

2.3. Results

2.3.1. Simulation with Brain Phantom

The proposed l_1 Bowsher prior recovered the detailed structure of the GM and tumors well even under high-level noise circumstances. Figures 2-3 and 2-4 show the representative reconstruction results for different noise levels (low and high) and patch sizes (10 and 20 voxels). Fifth regularization parameters (0.1×2^4 for l_2 Bowsher prior and 0.1×2^5 for others) were chosen for the visualization. The PET intensity in the large lesion was also less smeared with the proposed methods. Although the original Bowsher prior over-smoothed the small tumor, the proposed l_1 Bowsher prior methods preserved the shape and intensity of the small lesion. Figures 2-5 and 2-6 show the bias map for different noise levels (low and high). The proposed methods yielded lower bias under both low and high-level noise circumstances. Moreover, the bias of artificial lesions, especially for small lesion, were lower in the iteratively reweighted l_1 Bowsher prior than all the other reconstruction methods. This phenomenon also can be observed in the bias-STD plot (Figure 2-7) for each simulated region (Gray matter, white matter, large lesion and small lesion). Both the bias and STD were suppressed by the proposed l_1 Bowsher prior methods as the regularization parameter increases, however, the bias became greater with l_2 Bowsher prior. The bias for artificial lesions with iteratively reweighted l_1 Bowsher prior yielded the lowest value. This result was consistent

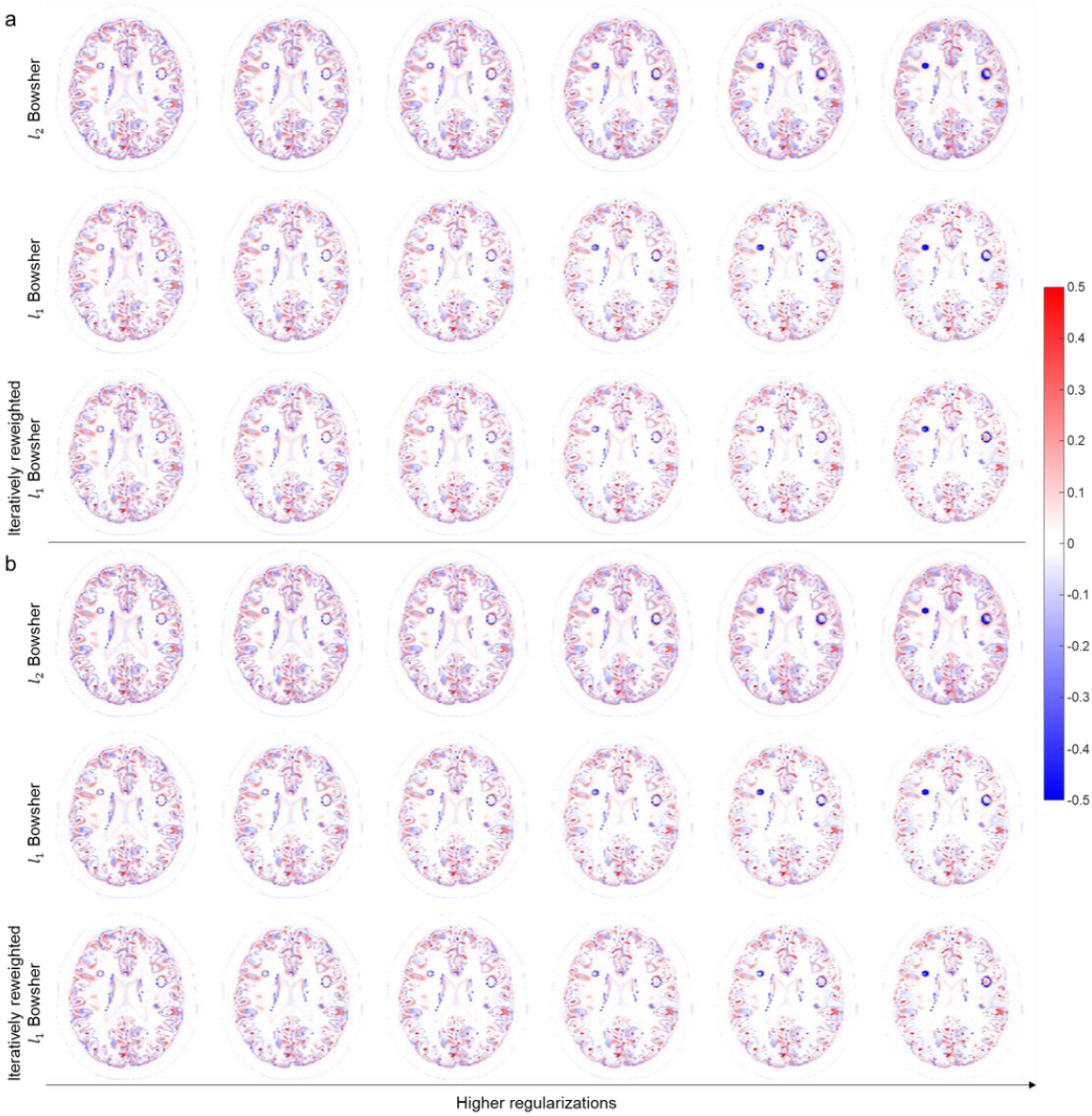

Figure 2-5. Bias map of computer simulation results using original $\boldsymbol{l_2}$ Bowsher prior, proposed $\boldsymbol{l_1}$ Bowsher prior and its iterative reweighting variation under the low-level noise circumstances (total 7.0×10^7 prompt counts). a. 10 voxels selection in the given patch (nearest 80 voxels) and b. 10 voxels selection in the given patch.

regardless of the noise level.

2.3.2. Human Data

As described in the Methods section, 20 voxels were selected in the patch for all reconstruction, which showed the better performance. With respect to the human data, the proposed l_1 Bowsher prior methods outperformed the original l_2 Bowsher

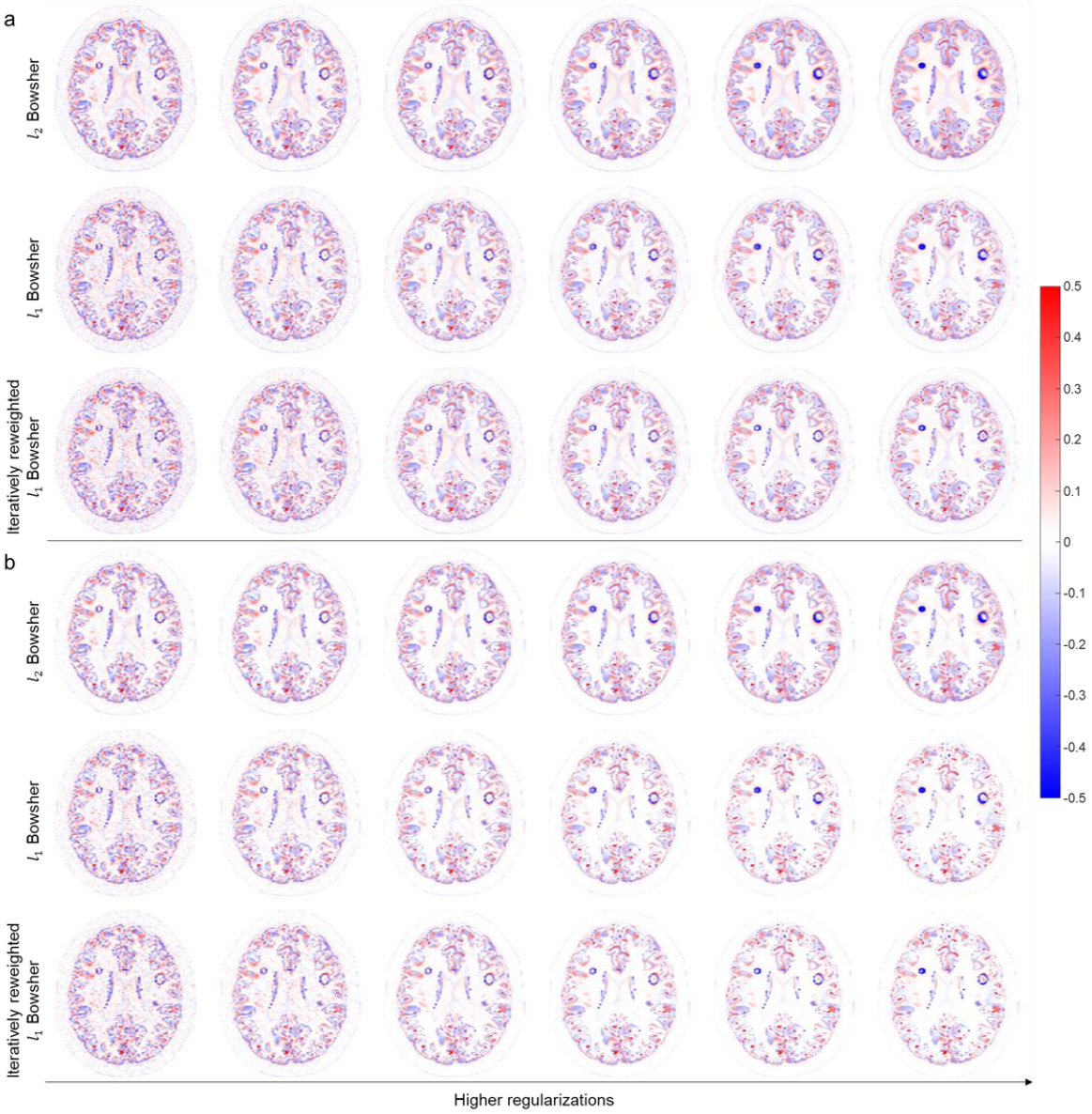

Figure 2-6. Bias map of computer simulation results using original l_2 Bowsher prior, proposed l_1 Bowsher prior and its iterative reweighting variation under the high-level noise circumstances (total 1.4×10^7 prompt counts). a. 10 voxels selection in the given patch (nearest 80 voxels) and b. 10 voxels selection in the given patch.

prior in preserving the detailed structures while suppressing the noise. As depicted in the [^{18}F]FDG PET image of the healthy volunteer (Figure 2-8), the original l_2 Bowsher prior with high regularization parameters yielded a blurred shape and decreased the uptake in some gyri, as highlighted with red boxes, and most subcortical regions, such as in the striatum. However, the proposed l_1 Bowsher

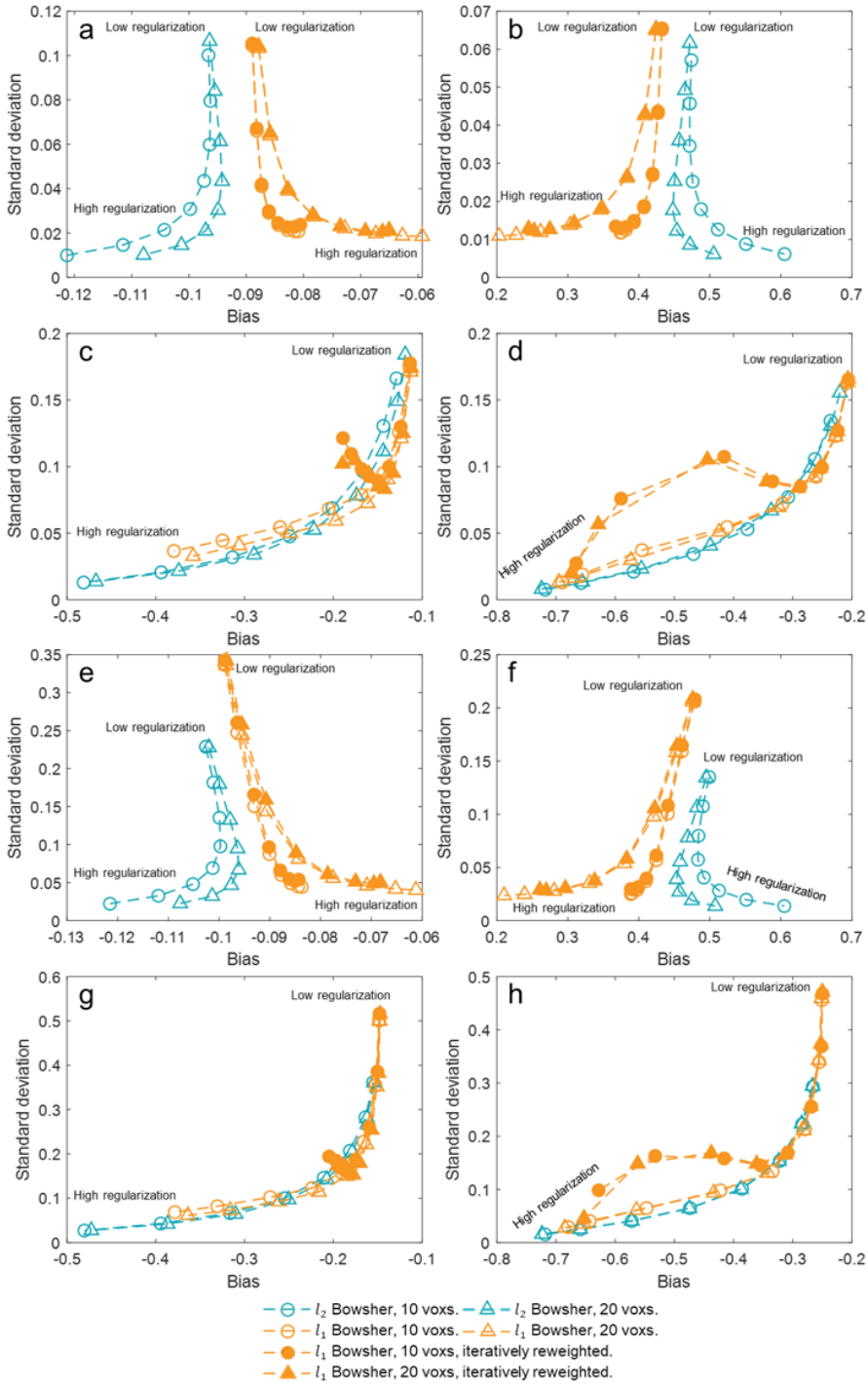

Figure 2-7. Bias-STD plot of computer simulation results using original $\boldsymbol{l_2}$ Bowsher prior, proposed $\boldsymbol{l_1}$ Bowsher prior and its iterative reweighting variation for four regions and two noise levels. a. Gray matter (GM) for low-level noise, b. white matter (WM) for low-level noise, c. large lesion for low-level noise, d. small lesion for low-level noise, e. GM for high-level noise, f. WM for high-level noise, g. large lesion for high-level noise and h. small lesion for high-level noise.

prior did not indicate such an adverse impact of the high regularization parameter.

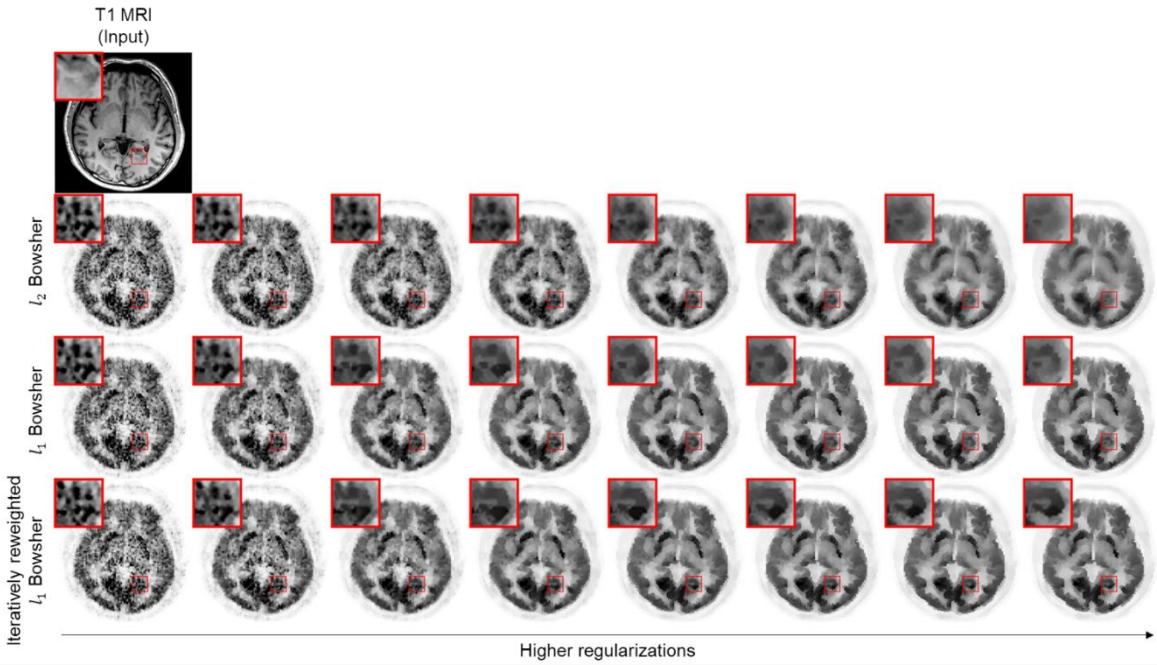

Figure 2-8. Reconstructed brain [^{18}F]FDG images of a healthy volunteer. The magnified region is highlighted by the red box.

These findings were confirmed in the quantitative analysis summarized in Figure 2-9 that shows the STD of uptake in white matter versus the mean uptake in four different gray matter regions (frontal lobe, cingulate cortex, superior parietal gyrus, and lateral temporal gyrus). Iteratively reweighted l_1 Bowsher prior showed higher uptake than other methods with similar STD. The uptake in the gray matter decreased as the regularization parameter increased when the original Bowsher prior was used. However, the uptake level was more constant with the l_1 Bowsher prior.

In addition, the l_1 Bowsher prior methods better preserved the increased PET uptake in the small lesion that was not visible in the structural T1 MRI used for the guiding anatomy as compared to the original Bowsher prior (Figure 2-10). It should be noted that the T2 MRI images presented in Figure 2-10 as supporting evidence of

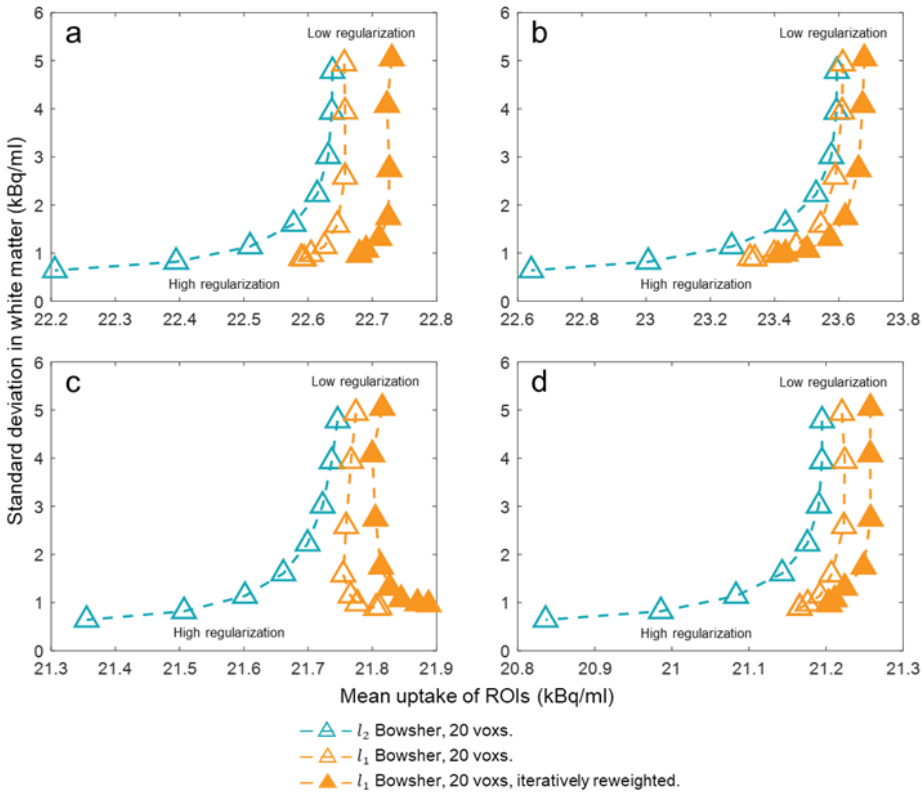

Figure 2-9. Quantitative analysis on four different regions in brain [^{18}F]FDG PET images. a. frontal lobe, b. cingulate cortex, c. superior parietal gyrus and d. lateral temporal gyrus.

the malignancy of the tumor were not used in the anatomy-guided reconstruction. Figure 2-11 depicts that the PET uptake in the small lesion is less impacted by the regularization parameter in the l_1 Bowsher methods, especially for the iteratively reweighting scheme.

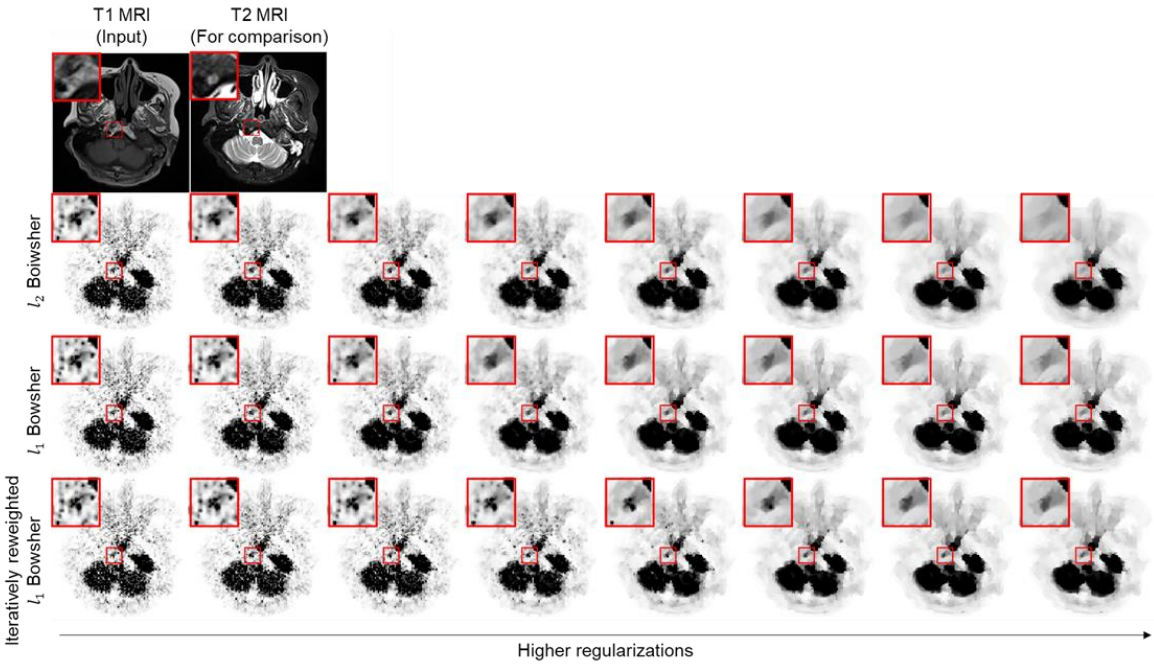

Figure 2-10. Reconstructed [^{18}F]FDG images of a head and neck cancer patient. Only T1 MR image was used for the anatomy-guided reconstruction.

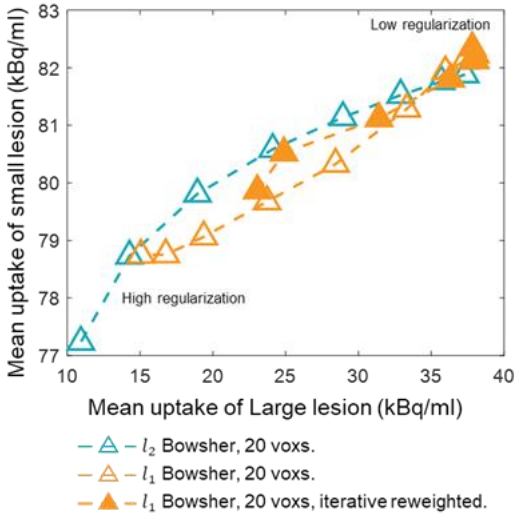

Figure 2-11. Quantitative analysis on two lesions in the head and neck [^{18}F]FDG PET images.

2.4. Discussions

In this study, we propose an MRI-guided regularized PET reconstruction based on a

new l_1 Bowsher prior and its application with the iterative reweighting scheme. In these methods, (13) plays a pivotal role in incorporating side information into the reconstruction process. The proposed proximal operator described in this equation is similar to the soft-thresholding operator used in the Lasso regression [55]. Both operators commonly cause the sparsity of their solution, leading to better detectability of small lesions.

As demonstrated by the simulation and real data, small lesions with abnormal PET uptake were better detected by the proposed l_1 Bowsher prior and its iterative reweighting variation as compared to the original l_2 Bowsher prior. The performance of the proposed method was particularly superior when such lesions are not shown in the MRI used for the regularized PET reconstruction (Figures 2-3, 2-4, and 2-10). The original l_2 Bowsher prior leads to smeared PET intensity in small lesions when there is no contact between the tumor and surrounding tissue in the anatomical prior. This is because, in (2) and (7), tumor voxels are not distinguishable based on the difference in voxels in the anatomical image. However, the proposed l_1 Bowsher prior enables to preserve the edges between the tumor and the surrounding tissue in PET because of the intrinsic edge-preserving property of the prior based on the l_1 norm. Moreover, Enhanced sparseness by iterative reweight enlarged this effect. For the same reasons, the proposed method works better than the original method when the MRI structures have a blurred boundary (striatum in Figure 2-8). In addition, the proposed method demonstrated smaller bias and less hyper-parameter dependency in PET intensity estimation in the regions (GM and WM) with matched anatomical boundaries in PET and MRI (Figures 2-5 and 2-6). The proposed l_1 Bowsher prior methods well preserve the mean uptake level of ROI even with the high regularization parameter although there is a trade-off

between the standard deviation and the mean uptake level of ROI in the original l_2 Bowsher prior.

Introducing iterative reweight scheme in the reconstruction with l_1 Bowsher prior yielded better quantification results compared to the vanilla l_1 Bowsher prior. It would be because, as mentioned above, the iterative reweighting enhances the sparseness of the prior. It originally aimed to approximate the optimization process from the l_1 relaxation to the l_0 minimization [36]. The sparsity of the intensity difference defined in (2) is important when the matched anatomical information is not provided because the uptake of these regions will be smoothed by the prior. However, if the optimization algorithm can preserve the sparseness, hot uptake surrounded by warm background can be preserved as shown in Figures 2-3, 2-4 and 2-10. However, promoting sparseness of the prior sometimes leads to a side effect. Under the high-level noise circumstance, it is not an easy task to distinguish noise and true signal in the image, resulting in worse denoising performance compared to the vanilla l_1 Bosher prior (Figure 2-10, second row). The ϵ is another control parameter and finding optimal settings including the number of patches and the number of selected voxels is a future direction of the research.

Although this is the first study to apply l_1-norm to the Bowsher prior as far as we know, the l_1-norm has been investigated extensively in the more general context of Bayesian (or penalized likelihood) image reconstruction. Various total variation (TV) minimization approaches have been proposed to improve the image quality of CT and emission tomography [21, 56-65]. In the most TV approaches, l1-norm of discretized gradient of image is used to regularize the fidelity optimization while preserving the edge information. In general, the TV-l_1 model suppresses noise in the uniform region more effectively than the l_2-norm regularization. However, TV-l_1

regularization often causes so-called "staircase" artifacts, yielding multiple flat regions separated by sharp boundaries. For PET images with high-level noise and low spatial resolution, the edges produced by TV prior might be inaccurate.

The shortcomings of the l_1-norm regularization could be alleviated by the anatomical prior because the edge-preserving property of the l_1-norm regularization is guided by the anatomical prior (Figure 2-12). However, the "staircase" artifacts still appears when the regularization parameter is high (Figures 2-8 and 2-10), so further investigations to mitigate the artifacts are needed. Another significant difference in this study from others is that the l_1-norm was applied to the Gibbs prior calculated using the distance between local neighboring pixels. Although many previous studies have used l_1-norm with TV prior [57, 66, 67], there are relatively few studies on l_1-norm regularization with other prior than TV for solving the inverse problems [68, 69]. Wang *et al*. applied l_1-norm directly to the solution vector and used the barrier function as well as the projection method to find the update equation. Liu *et al.* used both TV and l_1-norm of the image vector in the cost function, which is minimized by a fast iterative shrinkage-thresholding algorithm (FISTA) [47]. Both studies examined l_1-norm of the image vector, however, we modified potential function of the Gibbs prior from l_2-norm to l_1-norm. To minimize the proposed l_1 Bosher prior, modified proximal gradient was calculated and combined with the ordinary EM update.

A limited number of segmentation-free anatomy-guided reconstruction methods have been proposed so far. One of them is the kernel method that assumes that the PET image is a linear function of the transformed anatomical features from the MRI. The kernel-based method that encodes prior information into the PET projection model is another [32]. In this method, patch-based MR image features are

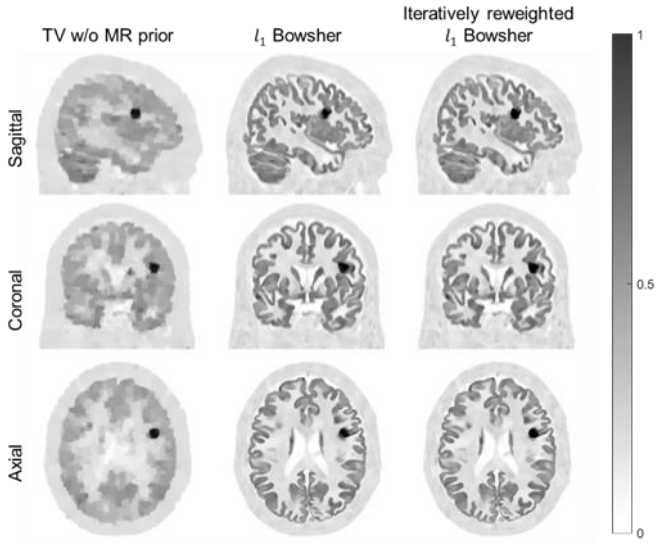

Figure 2-12. Comparison between TV prior using EM-TV algorithm (Sawatzky *et al.*) and l_1 Bowsher methods. Low count simulation data was used and the regularization parameter for TV prior was 4 and the others were the same with Figure 4 (0.1×2^5).

employed to form the kernel matrix. Because this kernel method incorporates anatomical information in the maxim likelihood formulation rather than in the penalized likelihood framework, it is amenable to ordered subsets. However, this approach also suffers from the over-smoothing of PET intensity in the regions where the PET uptake pattern differs from the anatomical side information. A parallel level set (PLS) prior between the anatomical and reconstructed PET image [18] is more robust to the discrepancy between the PET uptake pattern and anatomical side information. Nevertheless, using a differentiable prior requires well-defined parameter settings during the optimization process. Moreover, there is a report that the asymmetrical Bowsher prior shows better performance than the PLS method [22]. Our proposed method is also based on the Bowsher prior, but we have incorporated it into the edge-preserving property of the l_1 norm. The optimization of the cost function is easy to implement using the proximal gradient algorithm and the closed-form solution of the proximal operator. Similar to the original Bowsher prior, the

proposed method can be applied to multiple MRI pulse sequences. As presented in Figure 2-10, various MR images with various pulse sequences were acquired during routine PET/MRI studies. The weight used in (6) can be modified by combining information from the multiple MRI pulse sequences.

In this study, we applied the FORE algorithm to pre-corrected sinogram for scatter, random and attenuation to reconstruct real patient PET images using proposed prior models [52]. This would cause problems in terms of performance such as degraded sensitivity and resolution. However, the same optimization schemes can be used by replacing only the projection and backprojection parts with the 3D methods.

An approach to anatomy-guided functional image enhancement using deep neural networks is emerging, as deep learning is outperforming conventional approaches based on numerical and statistical signal processing in several different areas [38-41, 70-73]. Beyond simple noise reduction by recovering high-statistics PET images from the pair of anatomical image and low-statistics PET scan, more sophisticated concepts such as super-resolution and partial volume correction of PET are now being handled using deep learning [74-76]. Generation of anatomical images or the standard template from PET data using deep neural networks proposed for PET spatial normalization and attenuation correction [77-80] can be potentially utilized for reducing PET noise and enhancing its spatial resolution and image contrast. These methods have the potential for providing anatomical side information to be used for anatomy-guided PET image reconstruction. Including pre-trained deep neural networks that utilize anatomical side information for enhancing PET into PET-iterative reconstruction would also be an interesting future research topic [81-84].

Chapter 3. Deep Learning Approach for Anatomically-guided PET Reconstruction

3.1. Backgrounds

PET provides quantitative information on the spatiotemporal distribution of radiotracers that assess the functional and molecular changes in the body due to various diseases. However, PET has relatively low noise characteristics and spatial resolution than other anatomical imaging modalities, such as computed tomography (CT) or magnetic resonance imaging (MRI). As we explained in the previous chapters, a promising approach to improving the quality and quantitative accuracy of PET is incorporating MRI into the iterative reconstruction through anatomical information provided by MRI showing high contrast between soft tissues. [14, 17, 20, 22, 31, 33, 43]. In addition, the anatomically-guided PET reconstruction gains more attention than before, as the fully integrated simultaneous PET/MR scanner provides the spatially well-matched image pairs.

However, the simultaneous PET/MRI scanner is not available in most clinical and research centers. Besides, not all the patients who undergo PET/CT scans have corresponding MR images. Meanwhile, some analytic methods for iteratively solving equation (1) consist of a few proximal operators [46, 85, 86]. For example, we have shown that alternating use of proximal operator and EM update yields a solution for penalized Poisson log-likelihood with non-smooth Bowsher prior. Moreover, the MRI information is inserted during the calculation of the proximal operator. If we can substitute the proximal operator by learned neural network using the training set pair, the MR-less application of anatomy guided PET reconstruction

is achieved [87]. In this unrolled architecture, the forward and backward projectors were combined with a convolutional neural network. Some early papers proposed a similar neural network for CT denoising, SPECT denoising and penalized PET reconstruction [81, 88, 89]. Adler and Oktem proposed to use primal-dual hybrid gradient (PDHG) for unrolled neural networks and showed that the network provided better denoising performance than conventional PDHG, which required optimal parameter selection. The direct application of learned PDHG is not straightforward for PET image reconstruction due to Poisson statistics of the data and cost function, which is different from the CT reconstruction. Lim *et al*. used BCD-Net starting from the convolutional sparse coding algorithm. Although they showed improved performance than the existing iterative algorithms, the shape of the SPECT data used in the experiments is relatively simple compared to that of the brain PET. Mehranian *et al*. proposed a forward-backward splitting algorithm with shared network parameters for each iteration. They evaluated their network with U-Net [42]; however, because the number of network parameters was different, overfitting may occur for U-Nets with insufficient training data. In this study, we proposed to used Douglas-Rachford splitting for arbitrary convex regularization function. We examined two networks: an ordinary U-Net and an unrolled network containing conventional EM update modules in the convolutional neural network. The number of parameters for the two networks was approximately the same for the fair comparison.

3.2. Methods and Materials

3.2.2 Douglas-Rachford Splitting

Again, the penalized negative log-likelihood for PET reconstruction is given by:

$$\arg\min_{\boldsymbol{x}\geq 0} \sum_i \hat{y}_i(\boldsymbol{x}) - \boldsymbol{y}_i \log \hat{y}_i(\boldsymbol{x}) + \beta R(\boldsymbol{x};\boldsymbol{z}) \tag{21}$$

where $\boldsymbol{z}$ is the prior anatomical image (MRI). For arbitrary regularizer $R(\boldsymbol{x};\boldsymbol{z})$ which is convex, the iterative update of the solution is given by Douglas-Rachford splitting [46, 85]:

$$\boldsymbol{\omega}^{n+1} = arg\,\min_{\boldsymbol{\omega}} \sum_i \hat{y}_i(\boldsymbol{\omega}) - \boldsymbol{y}_i\, log\, \hat{y}_i(\boldsymbol{\omega}) + \frac{\rho}{2}\|\boldsymbol{\omega} - \boldsymbol{x}^n\|^2 \tag{22}$$

$$\boldsymbol{\nu}^{n+1} = arg\,\min_{\boldsymbol{z}} \beta R(\boldsymbol{\nu};\boldsymbol{z}) + \tfrac{\rho}{2}\|2\boldsymbol{\omega}^{n+1} - \boldsymbol{x}^n - \boldsymbol{\nu}\|^2 \tag{23}$$

$$\boldsymbol{x}^{n+1} = \boldsymbol{x}^n + (\boldsymbol{\nu}^{n+1} - \boldsymbol{\omega}^{n+1}). \tag{24}$$

The first equation (22) is the penalized PET reconstruction problem for quadratic prior and closed updated can be found using a separable quadratic surrogate (SQS) [45, 90]:

$$\boldsymbol{\omega}_{SQS}^{n+1} = arg\,\min_{\boldsymbol{\omega}} \sum p_j\left(\boldsymbol{\omega}_j - x_{j,EM}^{n+1}\, log\, \boldsymbol{\omega}_j\right) + \frac{\rho}{2}\|\boldsymbol{\omega} - \boldsymbol{x}^n\|^2 \tag{25}$$

$$\Rightarrow \boldsymbol{\omega}_{j,SQS}^{n+1} = \frac{1}{2}\left(\boldsymbol{x}_j^n - \frac{p_j}{\rho} + \sqrt{\left(\boldsymbol{x}_j^n - \frac{p_j}{\rho}\right)^2 + 4x_{j,EM}^{n+1}\frac{p_j}{\rho}}\right) \tag{26}$$

where $x_{j,EM}^{n+1}$ is the result of EM update and $p_j = \sum_i A_{ij}$ is the sensitivity vector for projection matrix. Although (26) is not the exact solution for (22), however, many studies showed that the SQS is well performed with various regularizers [13, 45]. The second equation (23) is the direct definition of proximal operator for regularizer R where the input is the $2\boldsymbol{\omega}^{n+1} - \boldsymbol{x}^n$. In the previous study with l_1-norm Bowsher prior, the proximal oprator is calculated based on the information of given MRI. If we can substitute the proximal operator to the learned neural network, the MR-less anatomy-guided PET reconstruction is achieved [87].

$$\mathrm{prox}_{R_{learned}}^{\beta\rho} = \arg_{R_\theta} \min_{\theta} L(f_{R_\theta,EM}(I), J) \tag{27}$$

L is the loss function used to train the network, I is an input image, J is a training target and θ is network parameters. By minimizing L in a supervised manner, the data-driven proximal operator is defined by the convolutional neural network.

3.2.1 Network Architecture

Figure. 3-1 shows the detailed structure of the unrolled deep neural network for the PET image reconstruction. Input to the network is PET sinogram and initially reconstructed PET image using the OS-EM algorithm (4 iterations and 21 subsets, 4-mm Gaussian post-filter).

The target is the anatomically-guided PET image that is reconstructed using the corresponding MRI and l_1 Bowsher prior. Once the network is trained, MRI is not necessary for the neural network-based PET image reconstruction. As shown in Figure 3-1, we used eight iteration blocks containing a single ordinary ML-EM

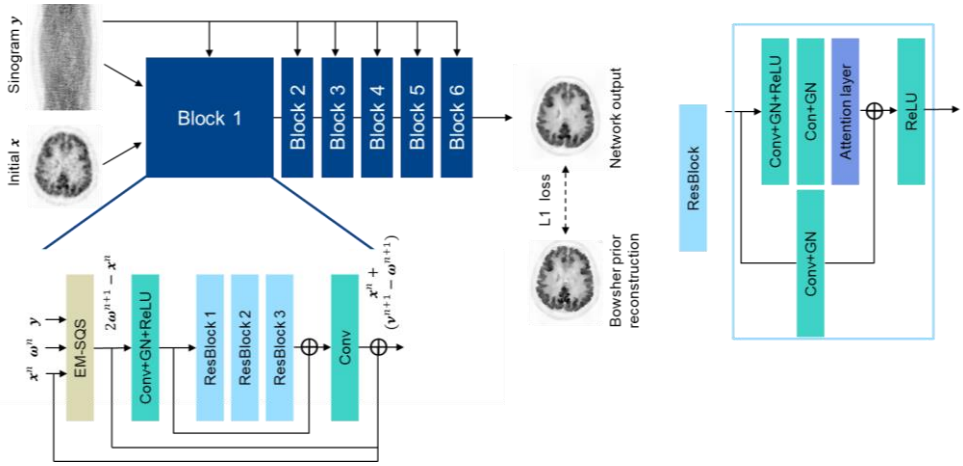

Figure 3-1. Schematic of the unrolled deep neural network for the MRI-less anatomically-guided PET image reconstruction.

update (forward and backward projections) followed by resNet subblocks with the attention layer.

For the comparison, we also trained a U-net with the same dataset. In the U-net that converts OS-EM image to the anatomically-guided PET based on Bowsher prior, 36 channels were used for the first layer to enable the fair comparison between the networks in terms of the parameter numbers. The total number of network parameters was 10.8M for the proposed network and 10.8M for the U-net. We fed both networks 2.5 images (adjacent three slices) as the channels to prevent the discontinuity in the orthogonal directions between axial slices.

3.2.2 Dataset and Training Details

We retrospectively used 39 [^{18}F]FDG brain PET scans acquired from a Biograph mCT 40 scanner (Siemens Healthcare, Knoxville, TN). The dataset was divided into the training (n=29) and test (n=10) sets. PET scan duration was 5 min and obtained after 110 min after injection of 5.18 MBq/kg of the radiotracer. Of the MRIs, only T1-weighted MR images were used for the regularized PET

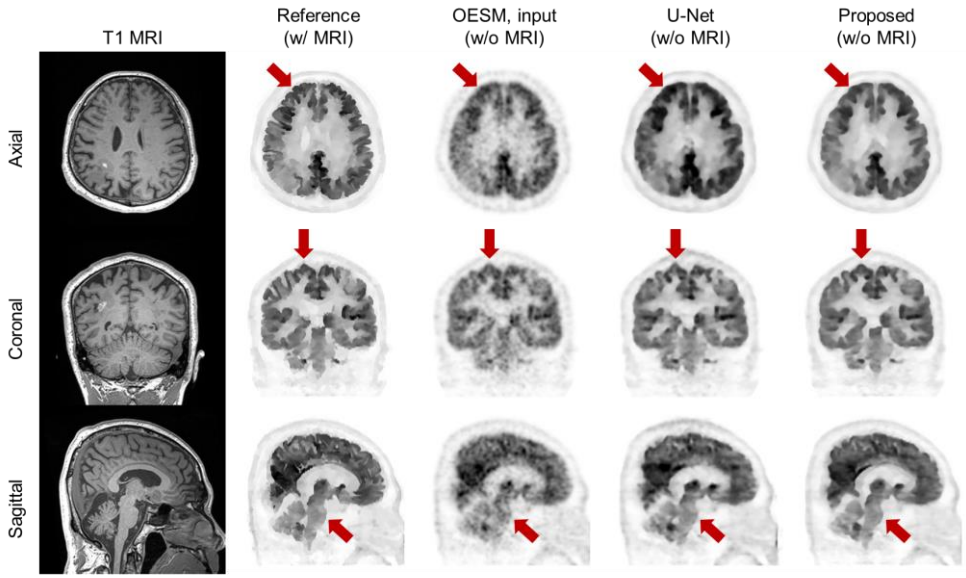

Figure 3-2. Reconstructed PET images of a representative case.

reconstruction. Retrospective use of all human data was approved by the Institutional Review Board (IRB) of our institute. Fourier rebinning algorithm (FORE) was used for the conversion of 3D sinograms to 2D. Both the proposed network and U-Net were optimized by the Adam algorithm. The learning rate was 0.0001. The batch size of the proposed network and U-Net was 1 and 8, respectively. We used L1 loss function for network training.

3.2.3 Image Analysis

Regional activity concentration in global gray matter regions was measured using an automated anatomical label (AAL) template after the spatial normalization using SPM12. The regional uptakes for 4 ROIs were extracted: frontal, cingulate, lateral temporal, lateral parietal. We calculated the error between the output of neural networks and the ground truth (Bowsher prior).

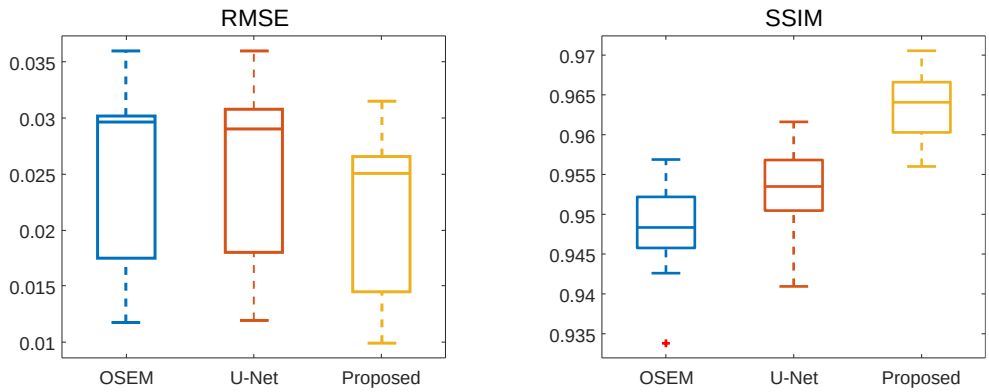

Figure 3-3. RMSE and SSIM for reconstruction methods for testset.

3.3. Results

Figure 3-2 shows the PET images reconstructed using Bowsher prior (reference), OSEM, U-Net, and proposed network. Our proposed network generated more consistent with the reference image than the U-Net. The gray matter uptakes were blurred and contaminated by the noise in the OSEM; however, the proposed network showed improved contrast between gray matter and surroundings. Although U-Net generates denoised images compared to OS-EM, however, the regional uptake is quite different from the reference. On the other hand, the proposed unrolled network showed denoised output and retained the regional uptake.

Figure 3-3 shows the result of RMSE and SSIM values for reconstruction methods. The RMSE value was slightly decreased for U-Net than OSEM; however, the variance was also increased. The proposed network shows the best performance than other methods for RMSE and SSIM.

Figure 3-4 shows the Bland-Altman plot of gray matter activity (Bq/ml, mean of four measured regions) between Bowsher prior and MR-less deep learning applications (U-Net and proposed unrolled network). Although the U-net approach's

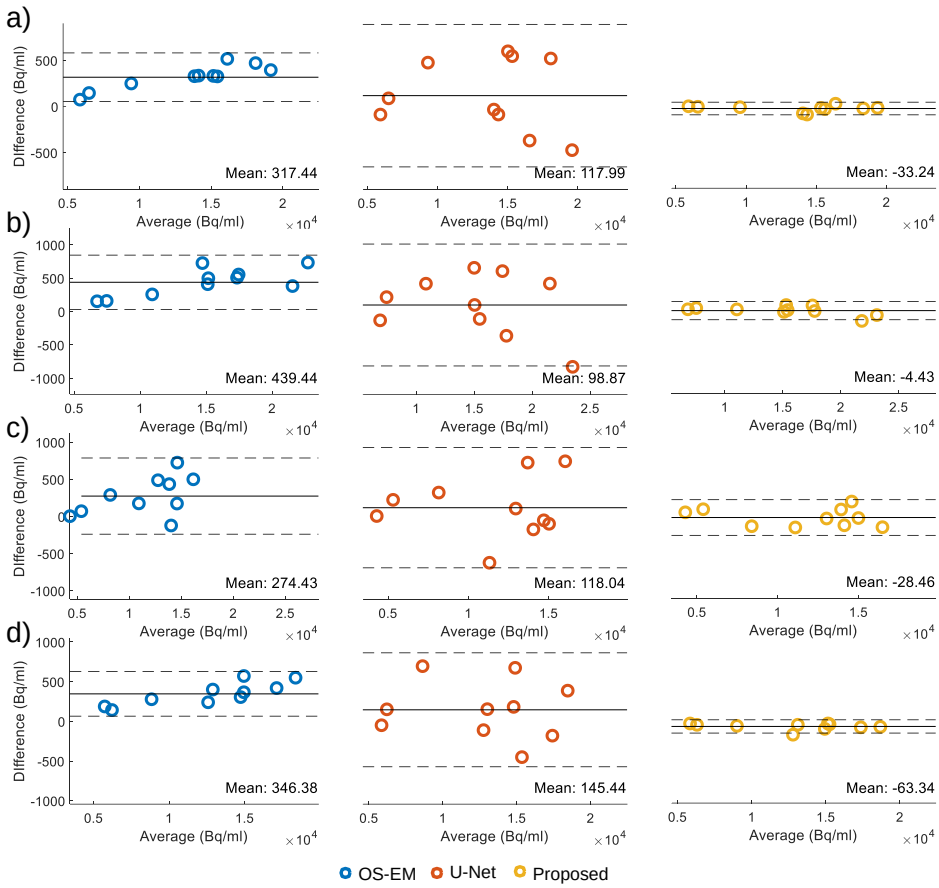

Figure 3-4. Bland-Altman plot of regional gray matter activity (Bq/ml) between Bowsher prior and deep learning methods (U-Net and proposed unrolled network). a. Frontal, b. cingulate, c. lateral temporal and d. lateral parietal. The mean difference is indicated in the figure.

quantification error was as high as 30%, the proposed unrolled neural networks yielded only small errors. The embedded ML-EM update in each block would prevent the deviation of uptake level from the observed data.

3.4. Discussions

In this study, we trained an unrolled deep neural network containing a conventional EM update module and compared it to the ordinary U-Net trained by an end-to-end manner. After training, both networks successfully generated denoised output and anatomical edges (e.g., the boundary between gray and white matter) were also

visually divided compared to the OS-EM. However, the U-Net results showed biased and more deviated distributions for the test set (Figure 3-3). In other words, it can be said that the generalization power of the network is weaker than the proposed unrolled network. The EM update module in the convolutional neural network compares the intermediate results with the sinogram and modifies them continuously (Figure 3-1).

The idea of unrolled networks starts with Algorithm 1. As we suggested above, the update equation for l_1 Bowsher prior consists of two alternating equations: EM update and proximal operator update. Here, the MRI information is only used to calculate the proximal operator. As a result, a neural network can be trained to produce an output similar to a proximal operator that guides and smoothes the image using an MR image. The trained network performs an anatomically guided PET reconstruction without MR. Experimentally, we show that the proposed unrolled network can learn the distribution of MRI information in the convolutional neural network.

Better generalization power than U-Net will probably be useful when using the training set and other test sets. For example, one can try amyloid positive PET images for the test, using the unrolled network trained only using amyloid negative PET images. Or, different radiotracers between training and test set could be examined. In this case, the distribution of training and test set is definitely different and ordinary single convolutional neural networks without EM modules are more likely to produce biased results (Figure 3-3). We would like to perform an additional experiment between various radiotracers.

Chapter 4. Conclusions

In this study, we proposed an l_1 norm-based Bowsher prior. The proximal gradient algorithm was exploited to solve the penalized likelihood function, and a modified proximal operator for EM-based reconstruction was provided. The iterative reweighting scheme enforcing sparseness of the prior improved both qualitative and quantitative results. The results from the computer simulation support the fact that our proposed methods yield a better quantification of tumors as well as the GM and WM than the previous approaches. Besides, clinical data showed that the proposed prior methods have a superior ability to detect small regions than the previous method. Therefore, these methods will help improve the PET image quality based on the anatomical information provided by other anatomical imaging systems. Nevertheless, further evaluations of the proposed method with more clinical data will be necessary.

Moreover, we also proposed to use deep neural networks combined with conventional EM module to generate MR-less anatomically-guided PET images. As we intended, the convolution layers successfully learned the distribution of target images that was clearly divided between anatomical edges and denoised in a homogeneous region. The regional analysis showed that the proposed unrolled network is less biased and deviated than the U-Net. In the future, we will evaluate our proposals for various radiotracers.

Bibliography

1. Wagatsuma, K., et al., *Comparison between new-generation SiPM-based and conventional PMT-based TOF-PET/CT.* Physica Medica, 2017. **42**: p. 203-210.
2. Shepp, L.A. and Y. Vardi, *Maximum likelihood reconstruction for emission tomography.* IEEE transactions on medical imaging, 1982. **1**(2): p. 113-122.
3. Lange, K. and R. Carson, *EM reconstruction algorithms for emission and transmission tomography.* J Comput Assist Tomogr, 1984. **8**(2): p. 306-16.
4. Qi, J. and R.M. Leahy, *Iterative reconstruction techniques in emission computed tomography.* Phys Med Biol, 2006. **51**(15): p. R541-78.
5. Louis, A.K. and F. Natterer, *Mathematical problems of computerized tomography.* Proceedings of the IEEE, 1983. **71**(3): p. 379-389.
6. Tikhonov, A.N. *On the solution of ill-posed problems and the method of regularization*. in *Doklady Akademii Nauk*. 1963. Russian Academy of Sciences.
7. Gourion, D. and D. Noll, *The inverse problem of emission tomography.* Inverse Problems, 2002. **18**(5): p. 1435.
8. Artzy, E., T. Elfving, and G.T. Herman, *Quadratic optimization for image reconstruction, II.* Computer Graphics and Image Processing, 1979. **11**(3): p. 242-261.
9. Hebert, T. and R. Leahy, *A generalized EM algorithm for 3-D Bayesian reconstruction from Poisson data using Gibbs priors.* IEEE transactions on medical imaging, 1989. **8**(2): p. 194-202.

10. Kaufman, L., *Maximum likelihood, least squares, and penalized least squares for PET.* IEEE Transactions on Medical Imaging, 1993. **12**(2): p. 200-214.

11. Fessler, J.A. and A.O. Hero, *Penalized maximum-likelihood image reconstruction using space-alternating generalized EM algorithms.* IEEE Transactions on Image Processing, 1995. **4**(10): p. 1417-1429.

12. Qi, J. and R.M. Leahy, *Resolution and noise properties of MAP reconstruction for fully 3-D PET.* IEEE transactions on medical imaging, 2000. **19**(5): p. 493-506.

13. Wang, G. and J. Qi, *Penalized likelihood PET image reconstruction using patch-based edge-preserving regularization.* IEEE transactions on medical imaging, 2012. **31**(12): p. 2194-2204.

14. Bowsher, J.E., et al., *Bayesian reconstruction and use of anatomical a priori information for emission tomography.* IEEE Transactions on Medical Imaging, 1996. **15**(5): p. 673-686.

15. Vunckx, K. and J. Nuyts. *Heuristic modification of an anatomical Markov prior improves its performance*. in *IEEE Nuclear Science Symposuim & Medical Imaging Conference*. 2010.

16. Bai, B., Q. Li, and R.M. Leahy, *Magnetic resonance-guided positron emission tomography image reconstruction.* Seminars in nuclear medicine, 2013. **43**(1): p. 30-44.

17. Tang, J. and A. Rahmim, *Anatomy assisted PET image reconstruction incorporating multi-resolution joint entropy.* Physics in medicine and biology, 2015. **60**(1): p. 31-48.

18. Ehrhardt, M.J., et al., *PET Reconstruction With an Anatomical MRI Prior*

Using Parallel Level Sets. IEEE Transactions on Medical Imaging, 2016. **35**(9): p. 2189-2199.

19. Novosad, P. and A.J. Reader, *MR-guided dynamic PET reconstruction with the kernel method and spectral temporal basis functions.* Physics in Medicine and Biology, 2016. **61**(12): p. 4624-4644.

20. Mehranian, A., et al., *PET image reconstruction using multi-parametric anato-functional priors.* Physics in Medicine & Biology, 2017. **62**(15): p. 5975-6007.

21. Knoll, F., et al., *Joint MR-PET Reconstruction Using a Multi-Channel Image Regularizer.* IEEE Transactions on Medical Imaging, 2017. **36**(1): p. 1-16.

22. Schramm, G., et al., *Evaluation of Parallel Level Sets and Bowsher's Method as Segmentation-Free Anatomical Priors for Time-of-Flight PET Reconstruction.* IEEE Transactions on Medical Imaging, 2018. **37**(2): p. 590-603.

23. Judenhofer, M.S., et al., *Simultaneous PET-MRI: a new approach for functional and morphological imaging.* Nature medicine, 2008. **14**(4): p. 459.

24. Yoon, H.S., et al., *Initial results of simultaneous PET/MRI experiments with an MRI-compatible silicon photomultiplier PET scanner.* Journal of Nuclear Medicine, 2012. **53**(4): p. 608-614.

25. Delso, G., et al., *Performance measurements of the Siemens mMR integrated whole-body PET/MR scanner.* Journal of nuclear medicine, 2011. **52**(12): p. 1914-1922.

26. Ko, G.B., et al., *Simultaneous Multiparametric PET/MRI with Silicon Photomultiplier PET and Ultra-High-Field MRI for Small-Animal Imaging.*

J Nucl Med, 2016. **57**(8): p. 1309-15.

27. Levin, C.S., et al., *Design features and mutual compatibility studies of the time-of-flight PET capable GE SIGNA PET/MR system.* IEEE transactions on medical imaging, 2016. **35**(8): p. 1907-1914.

28. Baete, K., et al., *Evaluation of anatomy based reconstruction for partial volume correction in brain FDG-PET.* Neuroimage, 2004. **23**(1): p. 305-317.

29. Baete, K., et al., *Anatomical-based FDG-PET reconstruction for the detection of hypo-metabolic regions in epilepsy.* IEEE transactions on medical imaging, 2004. **23**(4): p. 510-519.

30. Nuyts, J., et al., *Comparison between MAP and postprocessed ML for image reconstruction in emission tomography when anatomical knowledge is available.* IEEE transactions on medical imaging, 2005. **24**(5): p. 667-675.

31. Goffin, K., et al., *Anatomy-based reconstruction of FDG-PET images with implicit partial volume correction improves detection of hypometabolic regions in patients with epilepsy due to focal cortical dysplasia diagnosed on MRI.* European journal of nuclear medicine and molecular imaging, 2010. **37**(6): p. 1148-1155.

32. Hutchcroft, W., et al., *Anatomically-aided PET reconstruction using the kernel method.* Physics in Medicine & Biology, 2016. **61**(18): p. 6668.

33. Bowsher, J.E., et al. *Utilizing MRI information to estimate F18-FDG distributions in rat flank tumors*. in *IEEE Symposium Conference Record Nuclear Science 2004.* 2004. IEEE.

34. Chambolle, A., et al., *An introduction to total variation for image analysis.* Theoretical foundations and numerical methods for sparse recovery, 2010. **9**(263-340): p. 227.

35. Esser, E., *Applications of Lagrangian-based alternating direction methods and connections to split Bregman.* CAM report, 2009. **9**: p. 31.

36. Candes, E.J., M.B. Wakin, and S.P. Boyd, *Enhancing sparsity by reweighted ℓ 1 minimization.* Journal of Fourier analysis and applications, 2008. **14**(5-6): p. 877-905.

37. Ciresan, D., et al. *Deep neural networks segment neuronal membranes in electron microscopy images*. in *Advances in neural information processing systems*. 2012.

38. Krizhevsky, A., I. Sutskever, and G.E. Hinton. *Imagenet classification with deep convolutional neural networks*. in *Advances in neural information processing systems*. 2012.

39. Xie, J., L. Xu, and E. Chen. *Image denoising and inpainting with deep neural networks*. in *Advances in Neural Information Processing Systems*. 2012.

40. Simonyan, K. and A. Zisserman, *Very deep convolutional networks for large-scale image recognition.* arXiv preprint arXiv:1409.1556, 2014.

41. He, K., et al., *Deep Residual Learning for Image Recognition.* arXiv:1512.03385, 2015.

42. Ronneberger, O., P. Fischer, and T. Brox. *U-net: Convolutional networks for biomedical image segmentation*. in *International Conference on Medical image computing and computer-assisted intervention*. 2015. Springer.

43. Vunckx, K., et al., *Evaluation of Three MRI-Based Anatomical Priors for Quantitative PET Brain Imaging.* IEEE Transactions on Medical Imaging, 2012. **31**(3): p. 599-612.

44. Nuyts, J., et al., *A concave prior penalizing relative differences for*

maximum-a-posteriori reconstruction in emission tomography. IEEE Transactions on Nuclear Science, 2002. **49**(1): p. 56-60.

45. Sangtae, A. and J.A. Fessler, *Globally convergent image reconstruction for emission tomography using relaxed ordered subsets algorithms.* IEEE Transactions on Medical Imaging, 2003. **22**(5): p. 613-626.

46. Parikh, N. and S. Boyd, *Proximal algorithms.* Foundations and Trends® in Optimization, 2014. **1**(3): p. 127-239.

47. Beck, A. and M. Teboulle, *A fast iterative shrinkage-thresholding algorithm for linear inverse problems.* SIAM journal on imaging sciences, 2009. **2**(1): p. 183-202.

48. Cocosco, C.A., et al. *Brainweb: Online interface to a 3D MRI simulated brain database*. in *NeuroImage*. 1997. Citeseer.

49. BrainWeb. [cited 2019 04.30]; Available from: https://brainweb.bic.mni.mcgill.ca/.

50. An, H.J., et al., *MRI-based attenuation correction for PET/MRI using multiphase level-set method.* Journal of Nuclear Medicine, 2016. **57**(4): p. 587-593.

51. Kang, S.K. and J.S. Lee, *3D Inpainting of Brain MRI Using Deep Neural Networks*, in *2018 IEEE Nuclear Science Symposium and Medical Imaging Conference (NSS/MIC)*. 2018, IEEE: Sydney, Australia.

52. Defrise, M., et al., *Exact and approximate rebinning algorithms for 3-D PET data.* IEEE transactions on medical imaging, 1997. **16**(2): p. 145-158.

53. Tzourio-Mazoyer, N., et al., *Automated anatomical labeling of activations in SPM using a macroscopic anatomical parcellation of the MNI MRI single-subject brain.* Neuroimage, 2002. **15**(1): p. 273-289.

54. Ashburner, J. and K.J. Friston, *Unified segmentation.* Neuroimage, 2005. **26**(3): p. 839-851.

55. Tibshirani, R., *Regression shrinkage and selection via the lasso.* Journal of the Royal Statistical Society: Series B (Methodological), 1996. **58**(1): p. 267-288.

56. Rudin, L.I., S. Osher, and E. Fatemi, *Nonlinear total variation based noise removal algorithms.* Physica D: Nonlinear Phenomena, 1992. **60**(1): p. 259-268.

57. Sawatzky, A., et al. *Accurate EM-TV algorithm in PET with low SNR*. in *2008 IEEE Nuclear Science Symposium Conference Record*. 2008.

58. Guo, H., et al., *FDG–PET parametric imaging by total variation minimization.* Computerized Medical Imaging and Graphics, 2009. **33**(4): p. 295-303.

59. Ahn, S., et al., *Gap compensation during PET image reconstruction by constrained, total variation minimization.* Med Phys, 2012. **39**(2): p. 589-602.

60. Wang, C., et al. *Low dose PET reconstruction with total variation regularization*. in *2014 36th Annual International Conference of the IEEE Engineering in Medicine and Biology Society*. 2014.

61. Ehrhardt, M.J., P. Markiewicz, and C.-B. Schönlieb, *Faster PET reconstruction with non-smooth priors by randomization and preconditioning.* Physics in Medicine & Biology, 2019. **64**(22): p. 225019.

62. Niu, S., et al., *Sparse-view x-ray CT reconstruction via total generalized variation regularization.* Physics in Medicine and Biology, 2014. **59**(12): p. 2997-3017.

63. Gu, C., et al., *Promote quantitative ischemia imaging via myocardial perfusion CT iterative reconstruction with tensor total generalized variation regularization.* Physics in Medicine & Biology, 2018. **63**(12): p. 125009.

64. Burger, M., et al., *Total variation regularization in measurement and image space for PET reconstruction.* Inverse Problems, 2014. **30**(10): p. 105003.

65. Son, J., S.M. Kim, and J.S. Lee, *A strategy to reduce blocky pattern and contrast loss in emission tomography reconstruction with reduced angular sampling and total variation minimization.* Biomedical Engineering Letters, 2014. **4**(4): p. 362-369.

66. Beck, A. and M. Teboulle, *Fast Gradient-Based Algorithms for Constrained Total Variation Image Denoising and Deblurring Problems.* IEEE Transactions on Image Processing, 2009. **18**(11): p. 2419-2434.

67. Goldstein, T. and S. Osher, *The Split Bregman Method for L1-Regularized Problems.* SIAM Journal on Imaging Sciences, 2009. **2**(2): p. 323-343.

68. Wang, Q., et al., *Image reconstruction based on L1 regularization and projection methods for electrical impedance tomography.* Review of Scientific Instruments, 2012. **83**(10): p. 104707.

69. Liu, T., et al., *Regularized reconstruction based on joint L1 and total variation for sparse-view cone-beam X-ray luminescence computed tomography.* Biomedical Optics Express, 2019. **10**(1): p. 1-17.

70. Vincent, P., et al., *Stacked denoising autoencoders: Learning useful representations in a deep network with a local denoising criterion.* Journal of machine learning research, 2010. **11**(Dec): p. 3371-3408.

71. Agostinelli, F., M.R. Anderson, and H. Lee. *Adaptive multi-column deep neural networks with application to robust image denoising*. in *Advances in*

Neural Information Processing Systems. 2013.

72. Dey, D., S. Chaudhuri, and S. Munshi, *Obstructive sleep apnoea detection using convolutional neural network based deep learning framework.* Biomedical Engineering Letters, 2018. **8**(1): p. 95-100.

73. Mansour, R.F., *Deep-learning-based automatic computer-aided diagnosis system for diabetic retinopathy.* Biomedical Engineering Letters, 2018. **8**(1): p. 41-57.

74. Rigie, D., et al. *Approximating MRI-Based Anatomically Guided PET Reconstruction with a Convolutional Neural Network*. in *2018 IEEE Nuclear Science Symposium and Medical Imaging Conference Proceedings (NSS/MIC)*. 2018.

75. Song, T.-A., et al., *Super-resolution PET imaging using convolutional neural networks.* arXiv preprint arXiv:1906.03645, 2019.

76. Xu, J., et al., *200x low-dose PET reconstruction using deep learning.* arXiv preprint arXiv:1712.04119, 2017.

77. Choi, H. and D.S. Lee, *Generation of structural MR images from amyloid PET: Application to MR-less quantification.* Journal of Nuclear Medicine, 2018. **59**(7): p. 1111-1117.

78. Kang, S.K., et al., *Adaptive template generation for amyloid PET using a deep learning approach.* Hum Brain Mapp, 2018. **39**(9): p. 3769-78.

79. Hwang, D., et al., *Generation of PET attenuation map for whole-body time-of-flight 18F-FDG PET/MRI using a deep neural network trained with simultaneously reconstructed activity and attenuation maps.* Journal of Nuclear Medicine, 2019: p. jnumed. 118.219493.

80. Hwang, D., et al., *Improving the Accuracy of Simultaneously Reconstructed*

Activity and Attenuation Maps Using Deep Learning. J Nucl Med, 2018. **59**(10): p. 1624-1629.

81. Adler, J. and O. Öktem, *Learned primal-dual reconstruction.* IEEE transactions on medical imaging, 2018. **37**(6): p. 1322-1332.

82. Gupta, H., et al., *CNN-based projected gradient descent for consistent CT image reconstruction.* IEEE transactions on medical imaging, 2018. **37**(6): p. 1440-1453.

83. Kim, K., et al., *Penalized PET reconstruction using deep learning prior and local linear fitting.* IEEE transactions on medical imaging, 2018. **37**(6): p. 1478-1487.

84. Gong, K., et al., *Iterative PET image reconstruction using convolutional neural network representation.* IEEE transactions on medical imaging, 2018. **38**(3): p. 675-685.

85. Eckstein, J. and D.P. Bertsekas, *On the Douglas—Rachford splitting method and the proximal point algorithm for maximal monotone operators.* Mathematical Programming, 1992. **55**(1-3): p. 293-318.

86. Boyd, S., N. Parikh, and E. Chu, *Distributed optimization and statistical learning via the alternating direction method of multipliers*. 2011: Now Publishers Inc.

87. Meinhardt, T., et al. *Learning proximal operators: Using denoising networks for regularizing inverse imaging problems*. in *Proceedings of the IEEE International Conference on Computer Vision*. 2017.

88. Lim, H., et al., *Improved low-count quantitative PET reconstruction with an iterative neural network.* IEEE Transactions on Medical Imaging, 2020.

89. Mehranian, A. and A.J. Reader, *Model-based deep learning PET image*

reconstruction using forward-backward splitting expectation maximisation. IEEE Transactions on Radiation and Plasma Medical Sciences, 2020.

90. Erdogan, H. and J.A. Fessler, *Ordered subsets algorithms for transmission tomography.* Physics in Medicine & Biology, 1999. **44**(11): p. 2835.

Abstract in Korean (국문 초록)

양전자방출단층촬영 / 자기공명영상 (PET/MRI) 동시 획득 기술의 발전으로 MR 영상을 기반으로 한 해부학적 사전 함수로 정규화 된 PET 영상 재구성 알고리즘에 대한 심도있는 평가가 이루어졌다. 해부학 기반으로 정규화 된 PET 이미지 재구성을 위해 제안 된 다양한 사전 중 2차 평활화 사전함수에 기반한 Bowsher의 방법은 때때로 세부 구조의 과도한 평활화로 어려움을 겪는다. 따라서 본 연구에서는 원래 Bowsher 방법의 한계를 극복하기 위해 l_1 norm에 기반한 Bowsher 사전 함수와 반복적인 재가중치 기법을 제안한다. 또한, 우리는 이 매끄럽지 않은 사전 함수를 이용한 반복적 이미지 재구성에 대해 닫힌 해를 도출했다. 원래 l_2 와 제안 된 l_1 Bowsher 사전 함수 간의 비교 연구는 컴퓨터 시뮬레이션과 실제 데이터를 사용하여 수행되었다. 시뮬레이션 및 실제 데이터에서 비정상적인 PET 흡수를 가진 작은 병변은 원래 Bowsher 이전보다 제안 된 l_1 Bowsher 사전 방법으로 더 잘 감지되었다. 원래의 l_2 Bowsher는 해부학적 영상에서 병변과 주변 조직 사이에 명확한 분리가 없을 때 작은 병변에서의 PET 강도를 감소시킨다. 그러나 제안 된 l_1 Bowsher 사전 방법은 특히 반복적 재가중치 기법에서 l_1 노름에 의해 유도된 희소성에 기인한 특성으로 인해 종양과 주변 조직 사이에 더 나은 대비를 보여주었다. 또한 제안된 방법은 PET과 MRI의 해부학적 경계가 일치하는 영역에서 PET 강도 추정에 대한 편향이 더 낮고 하이퍼 파라미터 종속성이 적음을 보여주었다.

또한, l_1 Bowsher 사전 함수의 닫힌 해를 기반으로 기존의 ML-EM (maximum-likelihood expectation-maximization) 모듈을 포함하는 펼쳐진 네트워크도 제안되었다. 컨볼루션 레이어는 해부학적으로 유도 재구성된 PET 이미지의 분포를 성공적으로 학습했으며, EM 모듈은 중간 출력들을 사이노그램과 비교하여 결과 이미지가 잘 들어맞게 수정했다. 제안된 펼쳐진 네트워크는 지역의 흡수선량이 덜 편향되고 편차가 적어, 일반 U-Net보다 더 나은 성능을 보여주었다. 따라서 이러한 방법들은 해부학적 정보를 기반으로 PET 이미지 품질을 향상시키는 데 유용할 것이다.

주요어 : 이미지 재구성, 양전자방출단층촬영(PET), 해부학적 사전 함수, 딥 러닝, 펼쳐진 네트워크

학번 : 2014-22024